Faculty of Science
Institute of Geosciences
Remote Sensing, geoInformation and Visualisaiton
University of Potsdam

Master's Thesis
In Partial Fulfillment of the Requirements for the Degree of Master of Science

Applying Computed Tomography (CT) scanning for segmentation of permafrost constituents in drill cores

Damir Gadylyaev

Supervisors

Prof. Dr. Guido Grosse
University of Potsdam
Institute of Geosciences
Geological Remote Sensing

Prof. Dr. Julia Boike
Alfred Wegener Institute
Permafrost Research
Helmholtz Centre for Polar and Marine Research

15 October 2021

Acknowledgments

Abstract

Computed X-ray Tomography is a non-destructive technique that allows three-dimensional imaging of soil samples' internal structures, determined by their density and atomic composition variations. The objective of this thesis is to develop an image processing workflow for the quantitative analysis of ice cores using high-resolution CT to determine the volume fraction and vertical distribution of ice, mineral, gas, and organic matter in permafrost cores. I analyzed a 164 cm permafrost core taken from a Yedoma permafrost upland on Kurungnakh Island in the Lena River Delta (northeast Siberia). The obtained results were evaluated and compared with the results of detailed but sample-destructive laboratory analysis. The frozen permafrost core was subjected to a computerized X-ray imaging procedure with a resolution of 50 micrometers. As a result, I obtained 37000 images. Image segmentation was made with a multilevel thresholding method. Threshold values were determined based on the histograms of the images using Java-based image processing software (ImageJ). In addition, the vertical profiles were analyzed in 1-2cm intervals. Bulk densities and volumetric ice content (VIC) were received by freeze-drying and standard laboratory analysis. Here I show that the CT method cannot estimate pore ice in the silty permafrost material at the current resolution but can detect excess ice. CT method allows distinguishing well between ice-saturated mineral soil and organic matter. Automatic thresholding methods cannot obtain an accurate result and perform overall worse than the manual thresholding method. Comparison between CT and laboratory results shows that data derived from both methods overall demonstrate similar patterns but with different magnitudes. The image processing technique to quantify VIC provides a non-destructive analog to traditional laboratory analysis that could help increase the vertical resolution for quantifying mineral, ice, gas, and organic components in

permafrost cores and enhance the volumetric estimate.

Abstract (German)

Die Röntgen-Computertomographie ist eine Technik, die es ermöglicht eine dreidimensionale Darstellung, der inneren Strukturen von Bodenproben anzufertigen, ohne diese zu zerstören. Die innere Struktur wird, durch die durch die Variationen ihrer Dichte und atomaren Zusammensetzung bestimmt. Ziel dieser Arbeit soll es sein einen Bildverarbeitungsprozess für die quantitative Analyse von Eiskernen mit Hilfe hochauflösender Computertomographie zu entwickeln, um den Volumenanteil und die vertikale Verteilung von Eis, Mineralien, Gasen und organischem Material in Permafrostkernen zu bestimmen. Ich habe einen 164 cm langen Permafrostkern, entnommen von der Insel Kurungnakh im Lena-Flussdelta (Nordostsibirien) aus dem Permafrosthochland Yedoma. Die gewonnenen Ergebnisse wurden mit einer detaillierten, aber stichprobenartigen Laboranalyse verglichen. Der Permafrostkern wurde einem computergestützten Röntgenbildgebungsverfahren mit einer Auflösung von 50 Mikrometern unterzogen. Ich erhielt 37000 Bilder. Die Bildsegmentierung erfolgte mit einer mehrstufigen Schwellenwertmethode. Die Schwellenwerte wurden auf Grundlage der Histogramme der Bilder mit einer Javabasierten Bildverarbeitungssoftware (ImageJ) ermittelt. Zudem wurden die vertikalen Profile in Abständen von 1-2 cm analysiert. Schüttdichte und volumetrischer Eisgehalt (VIC) wurden durch Gefriertrocknung und Standard-Laboranalysen ermittelt. Mit dieser Arbeit zeige ich, dass die CT-Methode das Poreneis nicht im schlammigen Permafrostmaterial bei der gegebenen Auflösung nicht abschätzen kann, dafür kann man damit aber überschüssiges Eis nachweisen. Die CT-Methode ermöglicht eine gute Entscheidung zwischen dem eisgesättigtem Mineralboden und organischem Material. Automatische Schwellenwertverfahren können keine genauen Ergebnisse erzielen und schneiden insgesamt schlechter ab als das manuelle Schwellenwertverfahren. Der Vergleich zwischen CT- und

Laborergebnissen zeigt, dass die mit beiden Methoden gewonnenen Daten insgesamt ähnliche Muster aufweisen, wenn auch in unterschiedlichem Ausmaß. Die Bildverarbeitungstechnik zur Quantifizierung von VIC bietet ein zerstörungsfreies Pendant zur traditionellen Laboranalyse, das dazu beitragen könnte, die vertikale Auflösung für die Quantifizierung von Mineral-, Eis-, Gas- und organischen Komponenten in Permafrostkernen zu erhöhen und die volumetrische Schätzung zu verbessern.

Stichworte: Computertomographie; Bildverarbeitung; Gefriertrocknung; CT-Scan; Verarbeitungstechnik; Laboranalyse; Röntgen; Bildverarbeitungssoftware; Eisgehalt; zerstörungsfrei

Contents

List of Figures

List of Tables

Abbreviations and symbols

c_k	Cluster centers
d	Euclidean distance
EIC	Excess ice content
f	Unknown mixture distribution
h	Histogram value
J	Kullback-Lieber information distance
k	Number of clusters
M_b	Total weight of a bag
M_{dwb}	Total dry weight with a bag
M_{dw}	Total dry weight without a bag
M_m	Mineral weight
M_o	Organic weight
M_{wwb}	Total wet weight with a bag
M_{ww}	Total wet weight without a bag
N	Total numbers of pixels
$p(x, y)$	Input pixels
p_a	Air density

$\rho_{b(wet)}$	Dry bulk density
$\rho_{b(wet)}$	Wet bulk density
p_i	Ice density
p_m	Mineral grains density
p_o	Organic matter density
PIC	Pore ice content
q	Mixture fraction
T	Threshold
t	Thickness of a sample
Var	Variance
V	Volume
W_b	Weight of background pixels
W_i	Weights
W_f	Weight of foreground pixels
W_{top}	Water sitting on top of soil water
WL	Water loss
WCV	Within class variance
AEX	Aerials Express

AWI	Alfred Wegener Institute for Polar and Marine Research (German: Alfred-Wegener-Institut Helmholtz-Zentrum für Polar- und Meeresforschung)
cal BP	Calibrated years before the present
CT	Computed Tomography
DL	Deep Learning
ESRI	Environmental Systems Research Institute
FSA	Farm Service Agency
GIS	Geographic Information System
IC	Inorganic carbon
IGN	National Geographic Institute of France (French: Institut national de l'information géographique et forestière)
IPCC	Intergovernmental Panel on Climate Change
MET	Minimum Error Thresholding
MRI	Magnetic resonance imaging
NLM	Non-local means
NSIDC	National Snow and Ice Data Center
OC	Organic carbon
OLS	Ordinary least squares
PET	Positron emission tomography
RA	Regression Analysis
ROI	Region of Interest

SEM	Scanning Electron Microscopy
TC	Total carbon
TOC	Total organic carbon
USDA	United States Department of Agriculture
USGS	United States Geological Survey
VIC	Volumetric ice content
VMC	Volumetric mineral content
VOC	Volumetric organic content
WLS	Weighted Least Squares

1   Introduction

Due to a warming climate in the Arctic region, abrupt thawing of ice- and carbon-rich permafrost is expected. Permafrost is a part of the cryolithozone characterized by seasonal freeze and thaw of the upper layer. It is temperature-defined, so any ground that remains below 0°C for two consecutive years is considered permafrost (Harris, 1988 [1]). The extent of the permafrost region is around 21 million km^2, designating 22% of the entire Northern Hemisphere's exposed land surface (Obu, 2021 [2]) and primarily distributed in the north of Alaska, Canada, Siberia, and Greenland. Northern hemisphere permafrost soils contain 1460-1600 Pg terrestrial organic carbon, which is equivalent to about twice the carbon currently in the atmosphere (Tarnocai, 2009 [3]; Hugelius, 2014 [4]). It is also known that permafrost thawing is going to accelerate because the Arctic temperatures are expected to increase at about twice the global rate (IPCC, 2019 [5]). Thawing permafrost releases methane (CH_4) and carbon dioxide (CO_2) into the atmosphere, contributing to additional warming (Richter-Menge, 2009 [6]; Schaedel, 2016 [7]). The release of greenhouse gases from permafrost is a consequence of and a driver for global warming. Further global warming may increase mobilization of ancient organic carbon, posing positive feedback on global warming. In addition to the emission of gases, the thawing of permafrost brings with it many different adverse consequences: both on a large scale - global climate, economics, and small scale - local biodiversity, people, water supply, infrastructure (Boike, 2012 [8]; Schneider von Deimling, 2020 [9]). Studying thawing permafrost is particularly important because once it is thawed, the ground loses volume, and subsidence occurs, which causes further destabilization.

Besides destabilization, when permafrost thaws, the ground ice distributed in the soil causes a massive influence on erosion processes, hydrology,

and development of landforms (van Huissteden, 2020 [10]). Availability of vast amounts of ground ice directly increases the susceptibility of soils to erosion and subsidence (van Huissteden, 2020 [10]). However, there are still considerable uncertainties in the carbon pool estimates for Yedoma deposits due to limited field data concerning ground ice, organic carbon content and distribution, and bulk density (Tarnocai, 2009 [3]; Schirrmeister, 2011 [11]). The permafrost core analyzed in this thesis was sampled from an ice-rich Yedoma permafrost upland on Kurungnakh Island, Lena River Delta, northeast Siberia (72°21'N; 126°16'E; Fig. 1.1). Yedoma is an organic-rich (about 2% carbon by mass) Pleistocene-age permafrost with ice content by volume of 50–90% (Zimov, 1997 [12]). This region is considered to be understudied, with a lack of knowledge regarding the vulnerability and feedback in a changing climate (Grosse, 2013 [13]). Kurungnakh Island is the easternmost portion of the structurally elevated western delta and rises up to 55 m above sea level (Morgenstern, 2011 [14]). The core was drilled by expedition members of Alfred Wegener Institute (AWI) and is 1.84 cm long (including the active layer), and has a diameter of 7.5 cm.

Despite the importance of permafrost landscapes globally, we lack an understanding of processes that lead to the thawing of permafrost, timing, and magnitude of the permafrost carbon feedback on the climate system (Schuur, 2013 [15]; Turetsky, 2019 [16]). In accordance with global climate models, permafrost degradation will affect almost fifty percent of all current permafrost in the northern hemisphere by 2100 (Boike, 2012 [8]). Although all permafrost is affected by warming and thawing, the thawing of ice-rich permafrost causes robust feedbacks to ground surface stability, hydrology, ecosystem functionality, and topography (Rowland, 2010 [17]). Exploration and analysis of the subsurface variability will enhance the prediction of the role of these landscapes in a warming climate (Sieweert, 2021 [18]). Further analysis of permafrost cores' physical, thermal, and geotechnical properties and ground ice distribution will help predict thaw processes and parameterize numerical climate models more accurately. Another reason for permafrost cores to be of interest is that ground

ice therein can be stored for an extended period, creating an enduring palaeoenvironmental archive.
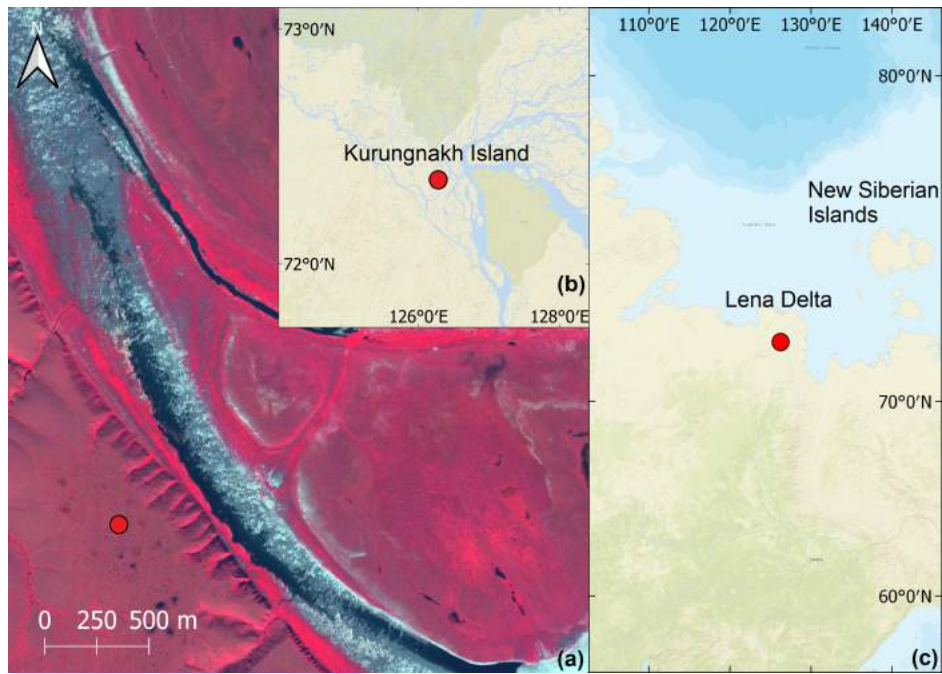
Figure 1.1: Study area **(a)** showing the core sampling site (image based on GeoEye-1); on **(b)** Kurungnakh Island in the eastern Lena delta; in **(c)** north-eastern Siberia. Panels **(b)** and **(c)** based on ESRI World Imagery. Sources: Esri, DigitalGlobe, GeoEye, i-cubed, USDA FSA, USGS, AEX, Getmapping, Aerogrid, IGN, IGP, swisstopo, and the GIS User Community

The National Snow and Ice Data Center (NSIDC) defines *ground ice* as a general term that refers to all types of ice contained in freezing and frozen ground. In this thesis, I differentiate between two types of ice - *excess ice* and *pore ice*. Excess ice (sometimes referred to as ground ice) is sited in amounts exceeding soil porosity in the forms of ice wedges and ice lenses. The amount of excess ice is vital since it can slow down

permafrost thaw (Lee, 2014 [19]). It is estimated that the presence of excess ice slows permafrost thaw with around a ten-year delay at 3 m depth at most high excess ice locations (Lee, 2014 [19]). Pore ice, in turn, is more subtle and amounts to less volume than excess ice, as it is ice that is occurring in the pores of soils and rocks. The ground becomes frozen ground when water situated in pores rocks, pebbles, soil - freezes. This frozen water is called *pore ice*. The difference between these two types of ice is related to the water content of the soil (Mackay, 1972 [20]). Once pore ice thawed, soil, bound together by pore ice, does not receive excess water, and therefore, thawing of pore ice causes no subsidence of the ground. On the contrary, with excess ice, the consequences of thawing are the opposite, and soil receives supernatant water (Mackay, 1972 [20]).

For the analysis of permafrost cores, they need to be drilled out (sampled), which is one of the most significant challenges infield practice for permafrost scientists (Calmels, 2005 [21]). Drilling into the permafrost and obtaining undisturbed and uncontaminated core samples is a nontrivial task because it may be difficult at higher latitudes in the continuous permafrost zone. This task requires a certain level of preparation, equipment, and skills. Being such a laborious job, it is quite understandable that these data are available from relatively few sites and do not represent the whole area. Considering the size of the territory and its inaccessibility, both from geographical and economical point of view, up to the present time, most researchers use not a volumetric but gravimetric ice content since they do not have cores or volumetric containers. This shortage is also related to difficult access to the currently perennially frozen soil layers (Zubrzyscki, 2012 [22]). It is particularly true for permafrost samples from a depth of more than 0.5 m (Zubrzyscki, 2012 [22]). After the sampling, the permafrost core was scanned by members of Helmholtz-Centre for Environmental Research - UFZ.

Further analysis of permafrost cores may include Computed Tomography scanning. The use of CT in geoscience in general, and in particular, to examine permafrost sediments, is rapidly gaining pace (Mees, 2003

[23]; Calmels, 2010 [24]; Cnudde, 2013 [25]). CT analysis has already established itself as a fast, reliable, non-destructible, and precise method that may also work both with macro and microstructures. This technology has been actively used for geoscientific needs since the early 1980s and has initially been principally developed for medical applications. As with any other method, CT scanning is not infallible. However, most possible errors are known and can usually be fixed during the image preprocessing step. Within the CT method, it is also possible to characterize soil cryostratigraphy. Classifying and identification of both cryotexture and cryostructure can explain the thermal history and origin of the substrate by which permafrost was formed and developed (Gilbert, 2016 [26]) because morphology, preservation, and formation of ground ice are all influenced by various environmental, climatic, and geologic factors (Katasonov, 2009 [27]; Murton, 2013 [28]). CT images obtained through scanning contain four easily distinguished fractions. I hypothesize that the image processing method should be able to segment the permafrost core into four constituents and quantify them. The image processing method has been subsequently strengthened with a statistical analysis method based on CT and laboratory data.

This thesis aims to contribute to a better understanding of the engagement between classical laboratory and CT methods. By discussing various physical and methodological approaches, the thesis aims to uncover both methods' advantages and limitations. Thus, the objectives set for the thesis:

- To estimate volumetric ground ice/water, mineral, gas, and organic matter content in permafrost sediment core using CT
- To compare the results of CT and laboratory analyses and evaluate physical and statistical differences between them
- Investigate the results and differences of various image processing techniques and settings

This research is based on an analysis of one permafrost core. However,

once the results are validated, the workflow could be used on the one hand for permafrost cores at other sites and, on the other hand, may contribute to discarding the unnecessary steps.

The thesis is structured as follows. Chapter 2 describes the whole methodology behind the analysis. Starting from sampling and scanning, it introduces the laboratory analyses workflow, image preprocessing and segmentation processes, and implementation of statistical approach. Chapter 3 presents the research results acquired in this study. Chapter 4 discusses the implications of the study results. Chapter 5 summarizes the final results and suggests possibilities for future research on the topic.

2   Methods

2.1 Sampling

In September 2017, during the field campaign, the permafrost core was mechanically drilled by members of the AWI expedition. Figure 2.1a shows the beginning of the sampling procedure with two scientists working with STIHL BT 121 by Andreas Stihl AG and a Sipre coring auger. Fig. 2.1b shows a part of the sampled core, from 20 cm to 102 cm approximately. The permafrost core analyzed in this thesis was taken from a plateau. The active layer thickness on the plateau was about 20 cm, which makes the total permafrost core length at about 1.64 cm. The diameter of the permafrost core was 7.5 cm. After the drilling, the permafrost core was transported under frozen conditions to the AWI Potsdam ice laboratory.

Figure 2.1: (a) Sampling coring with STIHL BT 121 in action; **(b)** The result of the sampling with visible transition from mixed phase into pure ice. Depth of the core part on a photo is approximately 20 cm to 103 cm. Photos: Julia Boike

2.2 Scanning

The permafrost core was scanned in February 2019 in the Helmholtz Center for Environmental Research. The scanning was performed with an X-ray microtomography system (XT H 225, Nikon Metrology (nikon-metrology.com)). The photo of the system and typical scanning material are presented in Fig. 2.2. The reconstruction of three-dimensional images was made with CT Pro 3D software (Nikon Metrology) at a spatial resolution of 50 μm and 8-bit grayscale resolution. An entire scan comprised 2000 projections. The total number of obtained images amounted to 37091.

Figure 2.2: Overview of scanning procedure **(a)** CT Nikon XT H 225 (nikon-metrology.com); **(b)** One of the cores inside the Nikon XT H 225 before scanning. Photo: Julia Boike

Computed X-ray tomography is a non-destructive (preserving sample integrity) technique that allows three-dimensional imaging of internal structures of the body, determined by variations in their density and atomic composition. CT scans are widely used for medical, geological,

industrial, and cultural needs. X-ray computed tomography uses X-rays and an electronic detector on the opposite side of the body to record a pattern of densities. The brightness of any part of an image is directly proportional to the attenuation of X-rays that pass through. The X-ray beam rotates around the object and takes multiple measurements to produce cross-sectional images of the body. The rotation distinguishes a CT scanner from a conventional X-ray that uses a fixed X-ray tube. As the X-rays leave the permafrost core, they are caught by the detectors and transferred to a computer (Fig. 2.3). Thus, the internal structure of the body can be reconstructed without destruction. After each completed turn, the computer reconstructs a 2D image slice. The reconstruction step has a significant impact on image quality (Lifeng Yu, 2016 [29]). However, users of CT scanners have finite control over the internal procedure of reconstruction. This control is limited to adjusting various parameters. In general, there is always a tradeoff between spatial resolution and noise for each kernel.
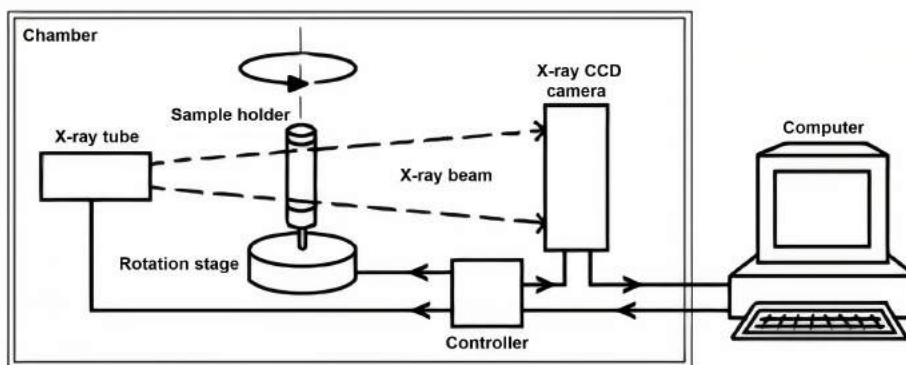
Figure 2.3: Schematic diagram of X-ray microtomography system. Image source: Tan, 2015 [30]

2.3 Laboratory analyses

In August 2020, the frozen core was cut into 1-2 cm pieces in the frozen laboratory of AWI Potsdam by members of the SPARC AWI team (Figure 2.4). Before the cutting procedure, all surfaces and saw blades were cleaned with ethanol. All members of the cutting team used sterile gloves all the time. A total of 66 samples were obtained.
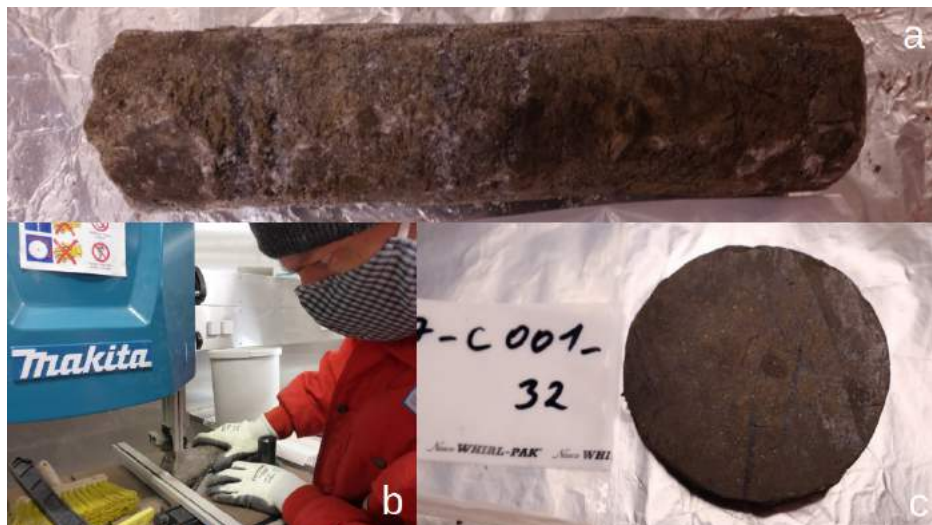
Figure 2.4: Work in the frozen laboratory. **(A)** one of the 164 cm core's parts in the laboratory; **(b)** cutting procedure performed by AWI member with chain saw blade; **(c)** sample example, the diameter is 7.5 cm. Photos: Julia Boike

We started cutting with a higher resolution. The average thickness of the first 12 samples was 0.9 cm, and the average volume of a sample was 39.9 cm^2. However, later we have changed the strategy and cut the rest coarser. The average thickness of the rest 54 samples was 1.9 cm, and the average volume of a sample was 85.8 cm^2. The diameter of all samples was the same - 7.5 cm. Each permafrost core sample was photographed from both sides, measured, weighed, and labeled. Table A1 in Appendix

provides detailed information regarding depth (start and end), thickness, diameter, and volume for all samples. Plastic bags were weighed and labeled as well. After the cutting procedure, all samples were stored in the freezer at a temperature of −15 °C.

The measurements of permafrost core samples directly in laboratory consisted of:

- Depth (start) [cm]
- Depth (end) [cm]
- Thickness [cm]
- Diameter [cm]

After the lab cutting procedure, further analyses were done in sediment and geochemistry laboratories from September to December 2020. The frozen soil samples were thawed at 100 °C and homogenized using a 2 mm sieve. After thawing, the meltwater was drained and extracted using rhizones and used to calculate the water loss. Followed by calculations of volumetric ice content, volumetric organic content (VOC), and volumetric mineral content (VMC). The whole laboratory workflow is depicted in Fig. 2.5.
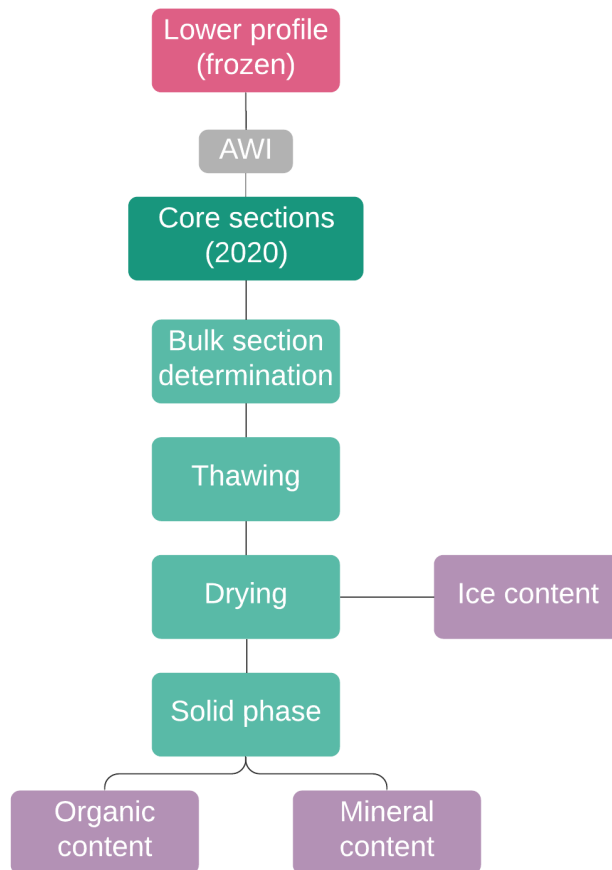
Figure 2.5: Flowchart of exploration and laboratory analyses of the samples

2.3.1 Bulk density

Bulk density is a property of soils and other masses of particulate material. It is the density of a volume of soil as it exists naturally; it includes air

space, organic matter, and soil solids (Mukhopadhyay, 2019 [31]). Unit of bulk density is the unit of weight over the unit of volume - [g/cm³]. Before thawing the samples, some of their bulk densities were quantified with the method of water displacement (Froeb, 2011 [32]).

The bulk density of soil, in this thesis, is determined from sampled permafrost core (Fig. 2.1); therefore, the total volume is known. From this sample, the wet bulk density ($\rho_{b(wet)}$ [g/cm³]) and the dry bulk density ($\rho_{b(dry)}$ [g/cm³]) can be determined. Wet bulk density consists of solid and liquid bulk densities. Both wet and dry bulk densities can be calculated as the weight of the soil particles divided by the total volume. Thus, the volume should be calculated first. Volume [cm³] was calculated accordingly to the cylinder volume formula:

$$V = \pi \cdot (d/2)^2 \cdot t \qquad (2.1)$$

where d is diameter [cm] that is the same for all the samples and equal to 7.5 cm;
t - thickness of the sample [cm];
π - mathematical constant Pi

Wet bulk density was calculated as follows: first, I calculated total wet weight without a bag (M_{ww}) [g] as:

$$M_{ww} = M_{wwb} - M_b \qquad (2.2)$$

where M_{wwb} - wet weight (incl. bag) [g];
M_b - weight of sample bag [g]

Thus, wet bulk density [g/cm³] can be calculated as follow:

$$\rho_{b(wet)} = M_{ww}/V \qquad (2.3)$$

Dry bulk density is calculated from wet bulk density [g/cm³], requiring several calculations. First I found dry weight (incl. bag) (M_{dwb}) [g]:

$$M_{dwb} = M_{wwb} - WL \tag{2.4}$$

where WL is water loss in [g] and is equal to wet weight - dry weight:

$$WL = M_{ww} - M_{dw} \tag{2.5}$$

Then I found dry weight without bag (M_{dw}) [g]:

$$M_{dw} = M_{dwb} - M_b \tag{2.6}$$

Thus, dry bulk density [g/cm³] can be found as follows:

$$\rho_{b(dry)} = M_{dw}/V \tag{2.7}$$

2.3.2 Volumetric ice content

Quantification of ground ice is vital for correct interpretation of permafrost systems and degradation modeling (Mollaret, 2020 [33]). However, until now, VIC is rarely estimated due to difficulties related to retrieving these data. In this thesis, VIC was determined both within the CT method and through laboratory analysis. This subsection focuses on laboratory-derived results. Volumetric ice content [cm³/cm³] was calculated as water loss [g] divided by volume [cm³] of the sample divided by ice density (916

kg/m³ [34]) divided by 1000 in order to convert it to g/cm³:

$$VIC = WL/V/(p_i/1000) \tag{2.8}$$

Similarly, I calculated excess ice content (*EIC*) [cm³/cm³] using W_{top} - water sitting on top of soil water instead of water loss [g]:

$$EIC = W_{top}/V/(p_i/1000) \tag{2.9}$$

Lastly, pore ice content (*PIC*) [cm³/cm³] was calculated simply as the difference between *VIC* and *EIC*:

$$PIC = VIC - EIC \tag{2.10}$$

2.3.3 Volumetric organic content

Permafrost soils and sediments contain a large assortment of organic materials. Yedoma permafrost is considered to be organic-rich permafrost soil and contains a considerable amount of currently frozen organic carbon (Strauss, 2014 [35]). The carbon in the Yedoma region is preserved well and available for decomposition after the thaw. In order to calculate VOC, first total organic carbon [wt%] (*TOC*) should be determined. The samples were measured two times with a *TOC* analyzer - Elementar Vario MAX C, a device with prebuilt inorganic carbon removal (Strauss, 2015 [35]). However, all TOC analyzers actually only measure total carbon (TC), while the determination of *TOC* requires calculations regarding inorganic carbon (IC) that is always there. This step was done with acidification of the sample to evolve carbon dioxide and measure it as IC.

Acidification was performed with 4% Hydrochloric acid.

Organic weight (M_o) [g] was calculated as:

$$M_o = TOC/100 \cdot M_{dw} \tag{2.11}$$

Volumetric organic content [cm³/cm³]:

$$VOC = M_{dw}/V/(p_o/1000) \tag{2.12}$$

2.3.4 Volumetric mineral content

With permafrost thawing, organic carbon (OC) stored in frozen deposits is unlocked and released. Simultaneously, mineral elements are unlocking as well. These elements interact with OC, causing OC stabilization and regulating methane and carbon dioxide emissions (Monhonval, 2021 [36]). Moreover, certain mineral elements are limiting the nutrients needed for the growth of plants and microbial metabolic activity (Monhonval, 2021 [36]). However, it is still unclear how exactly OC-mineral interactions will evolve, as permafrost will continue to thaw (Opfergelt, 2020 [37]). To calculate VMC, no new variables need to be introduced, and the workflow is similar to calculating VOC.

First, mineral weight (M_m) [g] was found as follows:

$$M_m = (1 - TOC/100) \cdot M_{dw} \tag{2.13}$$

Later, VMC [cm³/cm³] was found as:

$$VMC = M_{dw}/V/(p_m/1000) \qquad (2.14)$$

For validation of the results of volumetric contents, it is possible to check it with the sum of VIC, VOC, and VMC (volumetric fraction of air was ignored due to negligible volume). The result approaches one.

2.4 Image preprocessing

Image preprocessing is a common term for procedures related to correction, enhancement, restoration, and compression of raw images. Preprocessing aims to improve the images' quality and obliterate noise, missing, false or incomplete values. At the beginning of image preprocessing, I was working with raw image data, and at the end of this procedure, I received clean image data. Undoubtedly, image preprocessing alters the images and changes the final result. However, smart application of image preprocessing can benefit the outcome while taking care of images issues (Chaki, 2019 [38]). Preprocessing (along with image analysis and segmentation) was applied to the whole core length (163.7 cm). The complete image preprocessing workflow is shown in Fig. 2.6. Image preprocessing steps are shown in orange color. All of them were made on generated cross-sectional images with Java-based image processing software (ImageJ/FIJI (Schindelin, 2012 [39])).
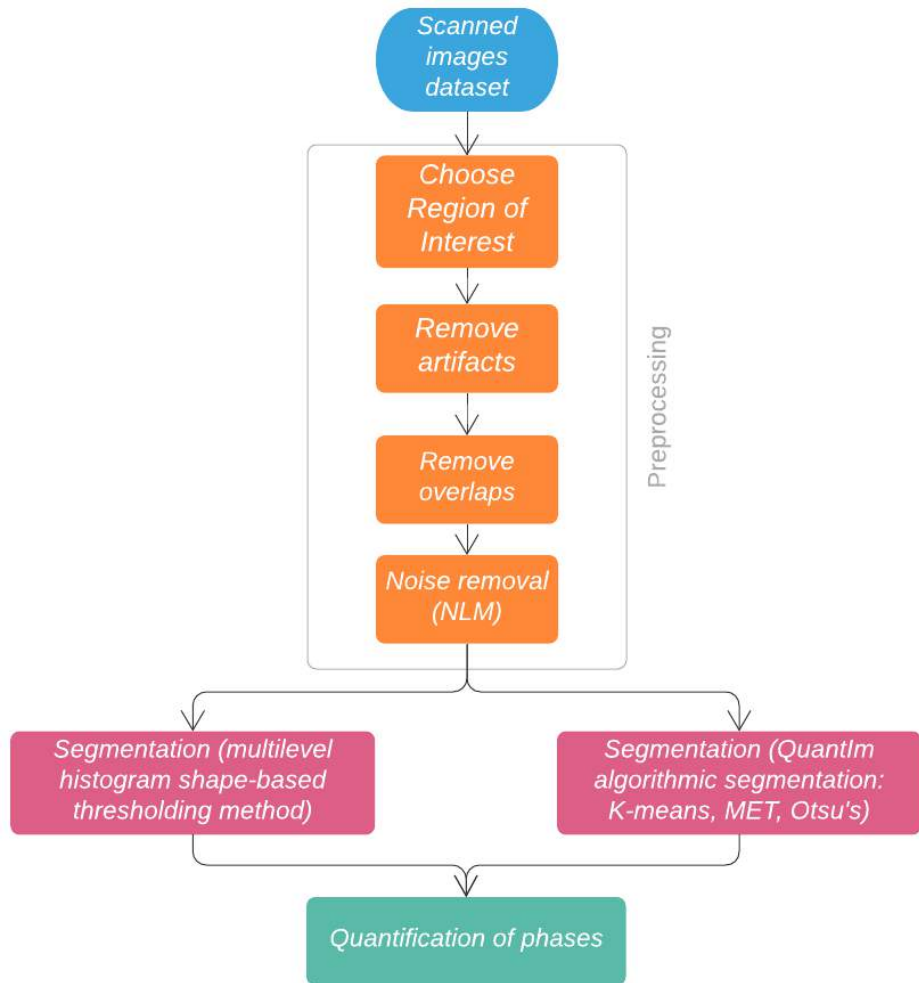
Figure 2.6: Image preprocessing steps conducted in this work

Overall, four image preprocessing steps were performed before the image analysis. The result of these image preprocessing steps is depicted in Fig. 2.7. This plot shows two versions of one random CT image, a raw one (Fig. 2.7a) and fully preprocessed (Fig. 2.7b).
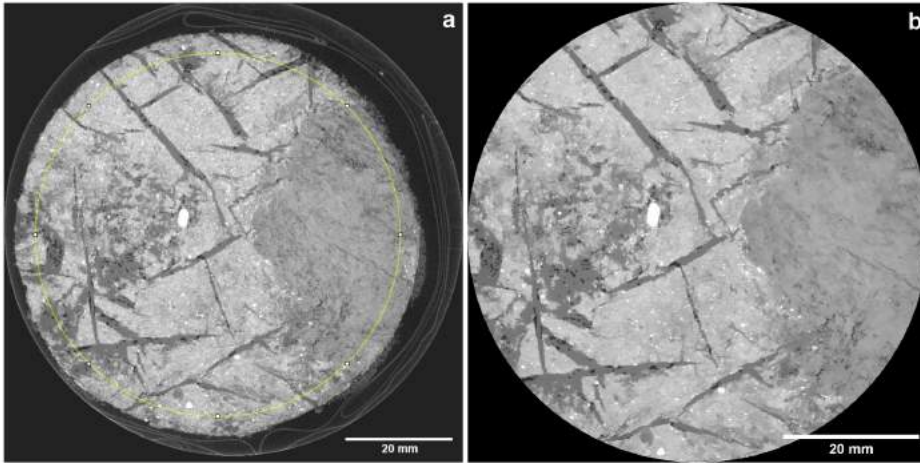
Figure 2.7: Overview of image preprocessing result, where **(a)** depicts random raw CT scan image and **(b)** is the same image but fully preprocessed and ready for the analysis

The first step was to choose a proper Region of Interest (ROI). The diameter of the core was 7.50 cm. However, the edges of each core were raggy and uneven and did not represent a perfect circle. Therefore, individual ROI was chosen for each scanned piece (image stack). The main criteria in ROI selection were to choose the surface as big as possible but without artifacts that may appear on the edge of the scanned image. The second image preprocessing step consisted of removing artifacts. A certain small amount of images have been fully affected by artifacts and were obliterated. These artifacts appeared solely due to drilling/packing procedures and have a mechanical origin. There were no difficulties with shadows of the objects and illumination unevenness. During the third image preprocessing step, overlaps between different scans were removed. Overlaps appeared since the scanner's detector was shorter than most permafrost core pieces. Hence each core was scanned several times, thus creating overlaps. These overlaps were removed manually in ImageJ. The last image preprocessing step was a reduction of noise. Cleared images

were filtered with a *Non-Local Means filter* (noise standard deviation = 6, smoothing factor = 1). This filtering method takes a mean of all pixels in the image but uses only pixels similar to a target pixel.

2.5 Image segmentation

Image segmentation is a generally used technique in digital image processing and analysis. It is based on dividing an image into different regions, where each region has certain properties. More precisely, each pixel has certain properties while regions consist of those pixels. There are various image segmentation techniques, including edge detection segmentation, region-based segmentation, clustering segmentation, CNN-based segmentation based on weakly-supervised learning in CNN, and others (Yuheng, 2017 [40]). In this thesis, I used thresholding-based segmentation and located boundaries. The first step for the segmentation of images is to determine the exact number of classes. The number of classes depends on the number of constituents. The density of any constituent directly affects the attenuation of the X-rays that pass through it. Density also affects the brightness level. Table 2.1 shows densities of permafrost constituents.

Constituent	Density [kg/m^3]	Symbol
Air	1.2 (Talay, 1975 [41])	p_a
Ice	916 (Voitkovskii, 1960 [34])	p_i
Organic matter	250 - 1300 (Meijboom, 1995 [42])	p_o
Mineral grains	2650 (De Vries, 1987 [43])	p_m

Table 2.1: Densities of constituents of permafrost core

The organic matter density used for the laboratory analysis in this thesis was 1300 [kg/m^3] (Meijboom, 1995 [42]).

Two different techniques were used for the image segmentation step:

- algorithmic thresholding (K-means, Otsu's and minimum error thresholding) made in open source C++ library for scientific image processing QuantIm (www.quantim.ufz.de)
- multilevel histogram shape-based thresholding method made in Java-based image processing software ImageJ/FIJI

From the CT images, four diverse and distinct phases can be distinguished. Each phase is characterized by distinctive shades of gray and brightness level as well as different structural features. Initially, they were called A, B, C, D. These A, B, C, D constituents are often distributed unevenly within the core, and in such cases, the histogram does not contain distinct peaks. While working with thresholding methods, it is crucial to have information about the intensity characteristics of the objects, their sizes, and the number of different types of objects appearing in an image (Salem, 2010 [44]). It must be noted that the final result of segmentation within any thresholding method is always open for discussion and revision. In order to decide if the result of segmentation is correct and trustworthy, it is crucial to have an independent estimate in the first place. In this thesis, the laboratory measurements serve this purpose.

2.5.1 Automatic image thresholding methods

The first attempt to classify the CT images has been made with automatic image thresholding. Image thresholding is a common task in many computer vision and remote sensing applications. It is an effective and straightforward classification technique that can also be used to classify CT images. The classification is based on a specific characteristic of the pixels, usually the intensity value. Thresholding is used to extract an object from its background by assigning intensity value T (threshold) for each pixel in a way that each pixel is either classified as an object point or as a background point. This thesis uses three automatic thresholding methods: Otsu's, K-means, and minimum error thresholding (MET). Automatic thresholding for all three methods was made in QuantIm, a free

C++ library for scientific image processing.

Automatic image thresholding methods generally consist of following steps (different methods usually vary in the third step):
1. Process the input image
2. Get image histogram
3. Compute threshold values *T*
4. Replace pixels with white in regions, where saturation is greater than *T* and with black in regions, where saturation is lower than *T*

Otsu's method
The Otsu's thresholding method is named after its inventor Nobuyuki Otsu and is used for automatic image thresholding (Otsu, 1979 [45]). The main idea of the method is to find the threshold that minimizes the weighted within-class variance. Otsu's thresholding returns a single intensity threshold that separates pixels into two classes, foreground, and background. This automatic thresholding method iterates through all the credible threshold values and calculates the spread for the pixel levels in the foreground or background. The goal is to determine the threshold value where the sum of foreground and background spreads is at its minimum.

Algorithm of the method by Bangare (Bangare, 2015 [46]):
1. Compute histogram for a 2D image
2. Calculate foreground and background variances (measure of spread) for a single threshold

    a) Calculate weight of background pixels and foreground pixels

    b) Calculate mean of background pixels and foreground pixels

    c) Calculate variance of background pixels and foreground pixels

3. Calculate "within class variance"

The workflow:
1. Calculate the weight for background and foreground pixels:

2. Calculate the weight of background pixels and foreground pixels:

$$W(weight) = \sum_{i=1}^{n} W_i/N \qquad (2.15)$$

where weights W_i are the probabilities of two classes separated by threshold T;

N - total number of pixels,

3. Calculate mean:

$$\mu(mean) = ((h_1 \cdot W_1) + (h_2 \cdot W_2) + ... + (h_n \cdot W_n) + (h_n \cdot W_n))/\sum_{i=1}^{n} \qquad (2.16)$$

where h - histogram value

4. Calculate variance:

$$Var = (((h_1 - \mu)^2 \cdot W_1) + ((h_2 - \mu)^2 \cdot W_2) + ... + ((h_n - \mu)^2 \cdot W_n))/\sum_{i=1}^{n}$$
$$(2.17)$$

5. Calculate within class variance:

$$WCV = W_b \cdot V_b + W_f \cdot V_f \qquad (2.18)$$

K-Means

For the first time, K-means as a term was used by James MacQueen in 1967 (MacQueen, 1967 [47]). This method is based on the same criterion as Otsu's method and minimizes the within-class variance. However, usually, K-means is faster than Otsu's algorithm since the first method is a local optimal method, while Otsu's method is a computationally expensive algorithm of searching the optimal global threshold (Liu, 2009 [48]). Furthermore, K-means, unlike Otsu's, does not compute a gray-level histogram before running. However, both methods perform similarly in multilevel thresholding, with K-means being faster (Liu, 2009 [48]).

The workflow:
1. Select k points as the initial class centroids
   where k is the number of clusters
2. Assign each object to the class with the shortest distance between the object and the center of that class. The Euclidean distance d is calculated as:

$$d = p(x, y) - c_k \qquad (2.19)$$

   where p(x,y) are the input pixels;
   c_k is the cluster centers
3. When all objects have been assigned, recalculate the positions of the k centroids as follows:

$$c_k = 1/k \cdot \sum_{y \in c_k} \cdot \sum_{y \in c_k} \cdot p(x, y) \qquad (2.20)$$

4. Repeat second and third steps until the positions of centroids do not change anymore
5. Find thresholds from the final partition
6. Reshape the cluster pixels into image

K-means algorithm is not able to find the appropriate number of clusters, and usually, it is considered to be one of the main disadvantages of that method (Dhanachandra, 2015 [49]). Fortunately, in my case, I have that exact number.

Minimum Error Thresholding

The Minimum Error Thresholding method was proposed by J. Kittler and J. Illingworth in 1984 (Kittler, 1984 [50]). This algorithm assumes that the histogram consists of two Gaussian normally distributed classes of pixel intensities. By an iterative process, two normal distribution curves are defined to fit two classes of pixels in the histogram in order to minimize a specified classification error (O'Gorman, 2018 [51]). The

optimum threshold value is the threshold intensity T that minimize the Kullback-Lieber information distance J (Azhar, 2002 [52]):

$$J = \sum_{i=1}^{t} p(i) \log \left[\frac{p(i)}{f(i)} \right] \tag{2.21}$$

where $p(i)$ is the observed probability histogram, and f is the unknown mixture distribution containing two distributions of h_1 and h_2 with mixture fractions q_1 and q_2, respectively.

$$f(i) = q_1 h_1(i) + q_2 q_2(i) \tag{2.22}$$

One of the main advantages of MET is that it produces a strong separation of classes, including cases when one class size is significantly smaller than the other (O'Gorman, 2018 [51]). It is still possible even when more minor constituents cannot be visibly noticed from the histogram. At the same time, MET does not perform well working with noisy images and histograms that contain many spurious peaks (O'Gorman, 2018 [51]). However, in my case, the noise was not a significant source of errors.

2.5.2 Manual thresholding

Manual thresholding has been processed within histogram shape-based technique using ImageJ. However, for specific image stacks, some histogram peaks were barely noticeable (Fig. 2.8). A bi-modal distribution (two clear peaks) can be noticed on the depicted histogram of the random image. This problem mainly occurred with air due to the small size and small air concentrations in the core. However, it was not a problem for the manual thresholding method, as the human eye can easily distinguish different shades of air and ice.
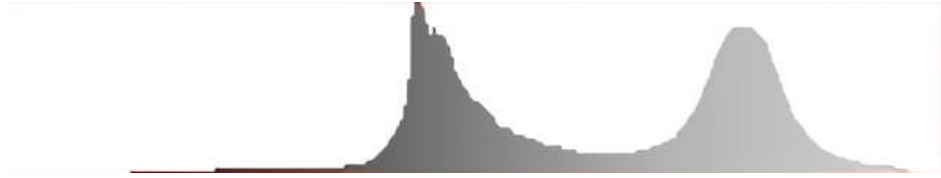
Figure 2.8: Histogram distribution of a random image with two clearly apparent peaks

Air has a low density and hence has a small attenuation. It is shown as a dark (black) color on a CT image (2.7). Ice has a higher density, so its color is brighter than the air's color. It is displayed as a dark gray color. The third constituent was labeled "Phase A" and presented as bright grey color. The fourth was labeled as "Phase B", and it is displayed as pure white color. Therefore, the full list of permafrost core constituents is:

- gas/*air*
- water/*ice*
- phase A
- phase B

2.6 Statistical method

Air/gas inclusions and pure (excess) ice can be identified with a high confidence level. However, there is no prior knowledge about the structure of the two remaining phases. Now suppose that they consist of saturated sediment, i.e., a mixture of organic sediment, mineral sediment, and (pore) ice. This assumption gives the following relations for the composition of phases A and B:

$$1 = \gamma_{A,i} + \gamma_{A,o} + \gamma_{A,m}$$
$$1 = \gamma_{B,i} + \gamma_{B,o} + \gamma_{B,m}$$

From the CT method the following variables can be computed:
- Excess ice (θ_{ei})
- Phase A (θ_A) that consists of pore ice fraction ($\gamma_{A,i}$), organic fraction ($\gamma_{A,o}$) and mineral fraction ($\gamma_{A,m}$)
- Phase B (θ_B) that consists of pore ice fraction ($\gamma_{B,i}$), organic fraction ($\gamma_{B,o}$) and mineral fraction ($\gamma_{B,m}$)

From the laboratory analysis the following independent measurements can be obtained:
- Volumetric gas content (θ_g)
- Volumetric ice content (θ_i)

    – Excess ice fraction (θ_{ei})

    – Pore ice fraction (θ_p)

- Volumetric organic content (θ_o)
- Volumetric mineral content (θ_m)

With these laboratory measurements, it is possible to apply regression analysis to compute such values of $\gamma_{A/B,i/o/m}$ that would give the best match between the CT analysis and the laboratory measurements. Regression analysis is a set of statistical methods for estimating relationships between a dependent variable (the main factor that I am trying to predict) and one or more independent variables (factors that presumably impact the dependent variable). In this case the dependent variable is laboratory measurements ($\theta_{i/o/m}$) and independent variables - CT images measurements ($\theta_{A/B/ei}$). CT measurements were averaged over the same depth-intervals ($j = 1..N_j$) as the samples from the laboratory.

The four fit parameters x_1-x_4 stand for:
- x_1 ($\gamma_{A,o}$) - organic fraction of phase A
- x_2 ($\gamma_{A,m}$) - mineral fraction of phase A
- x_3 ($\gamma_{B,o}$) - organic fraction of phase B

- x_4 ($\gamma_{B,m}$) - mineral fraction of phase B

Once we obtain coefficient values (x_1, x_2, x_3, x_4) it is possible to calculate ice fractions for phase A and phase B as follows:

$$\gamma_{A,i} = 1 - \gamma_{A,o} + \gamma_{A,m} \tag{2.23}$$

$$\gamma_{B,i} = 1 - \gamma_{B,o} + \gamma_{B,m} \tag{2.24}$$

Now using the values obtained through the CT analysis ($\theta_{A/B}(z_j)$) and the composition of the phases ($\gamma_{A/B,i/o/m}$), it is possible to calculate predicted values:

$$\theta_{i-pred}(z_j) = \theta_A(z_j) \cdot (1 - \gamma_{A,m} - \gamma_{A,o}) + \theta_B(z_j) \cdot (1 - \gamma_{B,m} - \gamma_{B,o}) + \theta_{ei} \tag{2.25}$$

$$\theta_{o-pred}(z_j) = \theta_A(z_j) * \gamma_{A,o} + \theta_B(z_j) \cdot \gamma_{B,o} \tag{2.26}$$

$$\theta_{m-pred}(z_j) = \theta_A(z_j) * \gamma_{A,m} + \theta_B(z_j) \cdot \gamma_{B,m} \tag{2.27}$$

Since laboratory estimates of the partitioning of the ice phase into pore ice and excess ice are avialable, they can be used to estimate pore ice content θ_{pi}:

$$\theta_{pi} = \theta_A(z_j) \cdot (1 - \gamma_{A,m} - \gamma_{B,o}) + \theta_{pi}(z_j) \cdot (1 - \gamma_{A,m} - \gamma_{B,o}) \tag{2.28}$$

In a similar way it is possible to calculate high resolution predicted values, the only difference is the number of data-points. Previously I used data from 53 core samples (lab data), now I am using the data from CT images (31275 data-points):
- Phase A ($\theta_{A,hr}$)
- Phase B ($\theta_{B,hr}$)

- Excess ice ($\theta_{ei,hr}$)

The calculations of high-resolution predicted values:

$$\theta_{m,pred-hr}(z_j) = \theta_{A,hr}(z_j) * \gamma_{A,m} + \theta_{B,hr}(z_j) \cdot \gamma_{B,m} \tag{2.29}$$

$$\theta_{o,pred-hr}(z_j) = \theta_{A,hr}(z_j) * \gamma_{A,o} + \theta_{B,hr}(z_j) \cdot \gamma_{B,o} \tag{2.30}$$

$$\theta_{i,pred-hr}(z_j) = \theta_{A,hr}(z_j) \cdot (1 - \gamma_{A,m} - \gamma_{A,o}) + \theta_{B,hr}(z_j) \cdot (1 - \gamma_{B,m} - \gamma_{B,o}) + \theta_{ei,hr} \tag{2.31}$$

Additionally, R squared values were calculated for each phase. R-squared is the measurement of how much of the independent variable is explained by changes in our dependent variables. In a nutshell, the value represents how well the regression line fits the data. The maximum value and also theoretically best value is 1. R squared have been calculated as follows (formulas are for organic fraction, mineral and ice fractions are calculated similarly):

The sum of squares of residuals:

$$SS\_res = \sum (\theta_o - \theta_{o-pred})^2 \tag{2.32}$$

The total sum of squares:

$$SS\_tot = \sum (\theta_o - \theta_{o-avg})^2 \tag{2.33}$$

R squared:

$$R^2 = 1 - SS\_res/SS\_tot \tag{2.34}$$

All statistical analyses were performed in Python within the Jupyter Notebook, an open-source web application (Kluyver, 2016 [53]).

3 Results

3.1 Thresholding methods

All CT images used for the analysis were processed without previous knowledge regarding the exact type of constituents. Although, the number of these constituents (classes) - four, have been chosen in advance. The image analysis algorithms were applied to the whole length of the core (163.7 cm). However, a random CT image has been chosen and visualized for a clearer understanding of the performance of varying image techniques and their differences. That image is situated at a depth of 56.6 cm and is shown in Fig. 3.1.

Figure 3.1: Segment of the permafrost core (20.3 - 102.0 cm) immediately after sampling. Red line represents the approximate position (56.6 cm) of CT image analyzed and visualized in Fig. 3.2 and Fig. 3.5

3.1.1 Automatic thresholding

Automatic thresholding was made with three methods - Otsu's, K-means, and MET. Fig. 3.2 provides an overall visual performance comparison for these three methods as well as for the manual thresholding method.
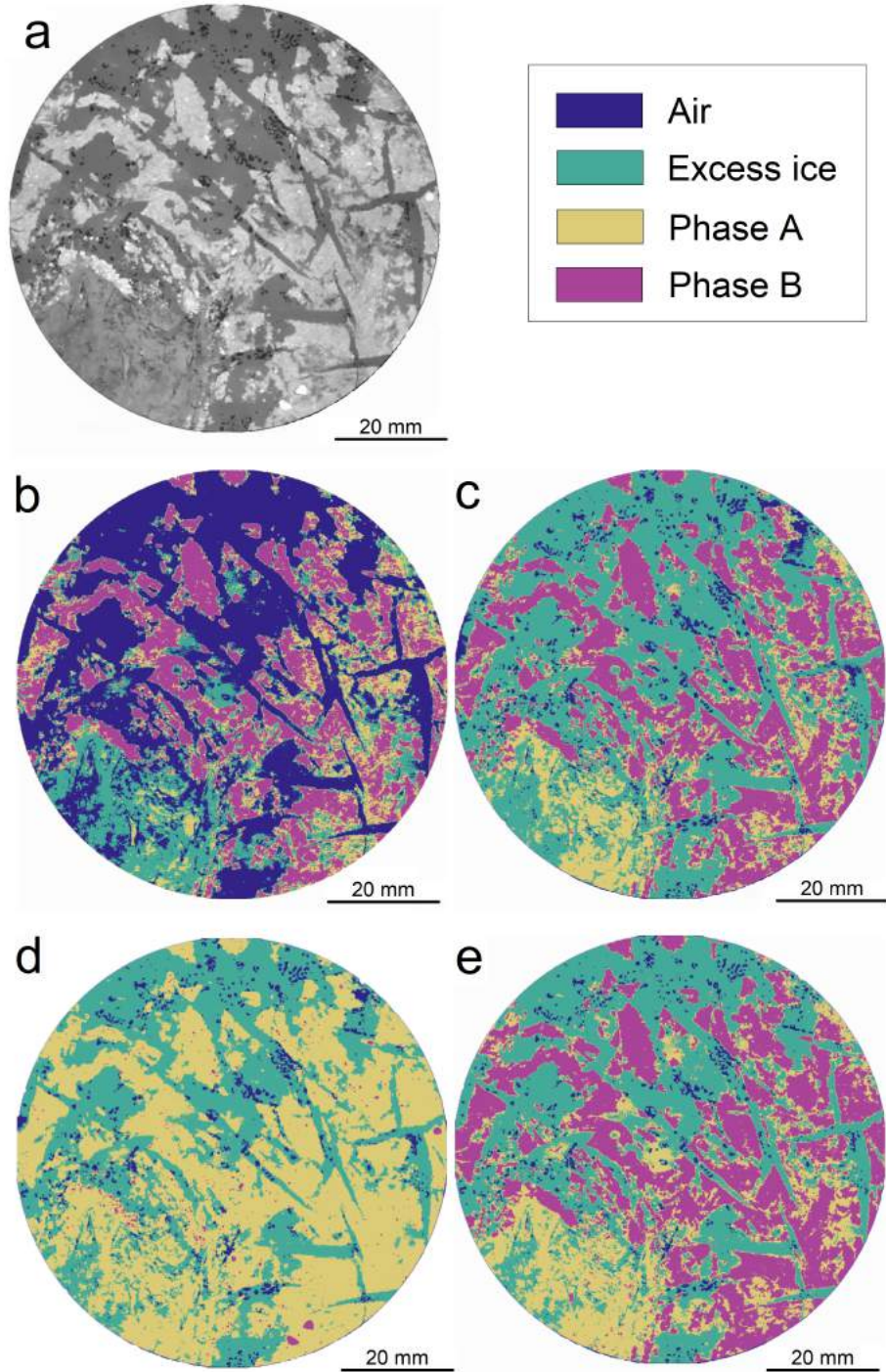
Figure 3.2: Comparison of performance of four thresholding segmentation methods on a random CT image taken from 56.6 cm depth. **(A)** CT image; **(b)** Otsu's; **(c)** K-means; **(d)** MET; **(e)** Manual

The four methods segmented CT image from Fig. 3.1. Determination of threshold values has been done with ImageJ preinstalled modules. Visualization was made in Python within the OpenCV library (Open Source Computer Vision Library (Bradski, 2008 [54]). Fig. 3.2a shows a randomly chosen CT image. Fig. 3.2(b, c, d, e) show the same image segmented by Otsu's, K-means, MET, and manual thresholding method, respectively. The obtained results differ considerably. The image segmented by Otsu's method (Fig. 3.2b) is covered at least by half with air. Which cannot be true according to a simple visual check of the CT image. The image segmented by MET method (Fig. 3.2d) is dominated by Phase A constituent. Meanwhile, images segmented by K-means (Fig. 3.2c) and Manual method (Fig. 3.2e) provide relatively similar result.

The previous figure (Fig. 3.2) shows segmentation results only for one particular image. However, it is beneficial to focus on a more significant core part for more excessive analysis. Fig. 3.3 shows the results for three different automatic thresholding methods (Fig. 3.3a, b, c) in comparison with the manual thresholding method (Fig. 3.3d) for 43.2 - 71.84 cm part of the permafrost core. That figure was created in Python using Plotly Python Open Source Graphing Library (Perkel, 2018 [55]). The segment shown in that figure, comprised of four pieces scanned individually. Although all pieces were scanned likewise, they still may have a different level of luminosity, and it directly affects the final composition result. This luminosity is expressed not in a sudden flash in a certain part of the certain image but a different overall brightness level between different scanned pieces (image stacks). This brightness level difference explains sudden abrupt artificial increase and decrease of constituents.
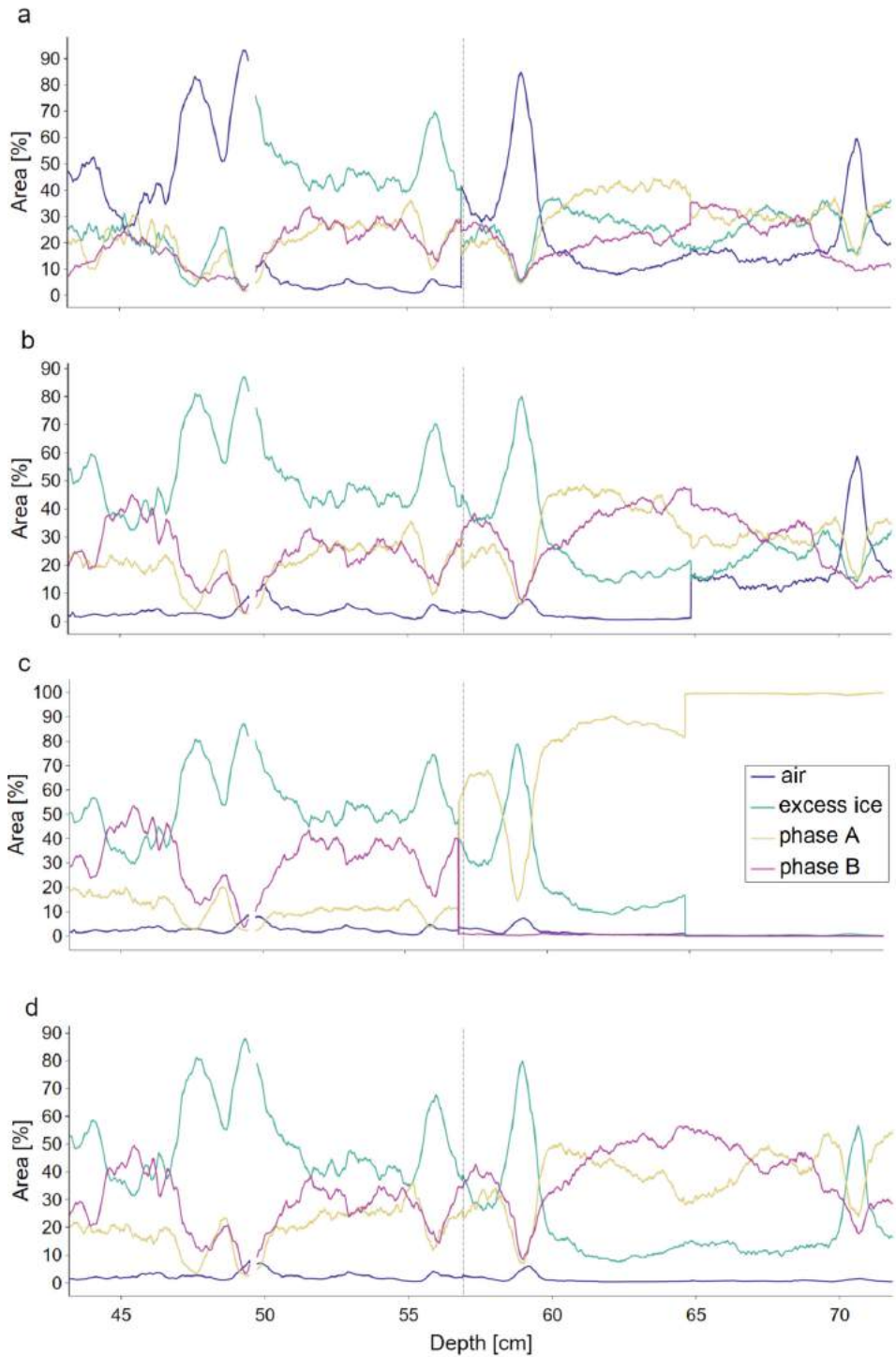
Figure 3.3: Partial (43.2 - 71.84 cm) segmentation results of four thresholding techniques **(a)** K Means; **(b)** MET; **(c)** Otsu's and **(d)** Manual thresholding method. The vertical black dotted line represents a CT image depicted in Fig. 3.2

Fig. 3.4 is a fraction of Fig. 3.3 and shows two apparent errors at two different spots of the previous figure. As described in the Methods part of the thesis, the core could not entirely fit into the CT system. Thus overlaps have been created. That overlap cannot be noticed in Fig. 3.4b that was made by manual thresholding method but can be clearly seen in in Fig. 3.4a made by K-means algorithm. In the right panel, another artifact can be seen. In this case, Fig. 3.4c was made with Otsu's method, and Fig. 3.4d with manual thresholding. There is a clear error in Fig. 3.4c where air and excess ice (blue and green lines) are mixed up, while Fig. 3.4d does not contain such a mistake. These errors happen because every image stack has different brightness levels and density occurrences are sample-specific. Therefore, their histograms vary greatly. Consequently, they are segmented differently.

Overall, automatic thresholding methods have explicit problems dealing with soil cores. That happens due to heterogeneous structure and uneven distribution of the constituents along with the core. The primary source of the errors for automatic methods is that the object area was often too small compared to the background area. Therefore, the image histogram is dominated by an extensive background area, increasing the probability of any pixel belonging to the background. Moreover, automatic thresholding methods are global. They are less suitable for obtaining the maximum information from the grayscale images (Iassonov, 2009 [56]).
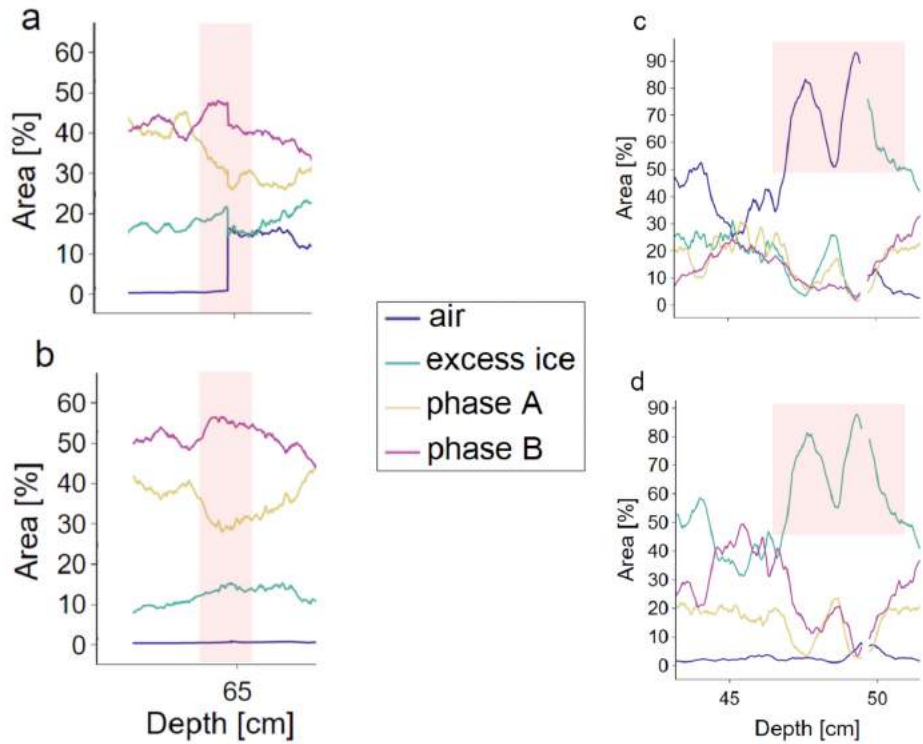
Figure 3.4: Examples of inconsistency and errors created within automatic thresholding by the case of Fig. 3.4 as well as results of manual thresholding free of these errors. Left panel **(a)** shows a wrong artificial abrupt increase (or decrease) of segmentation values made by K means algorithm, and **(b)** shows a segmentation result of the same spot made by manual thresholding, where such surges cannot be seen. The right panel **(c)** shows the error made by Otsu's method, air, and excess ice and mixed up, **(d)** shows the same spot free from that error

3.1.2 Manual thresholding

Fig. 3.5 serves to visualization purposes of the manual thresholding method and shows the segmentation result of the CT image from Fig. 3.2, its histogram, the laboratory sample the image belongs to, and laboratory analysis of that sample.
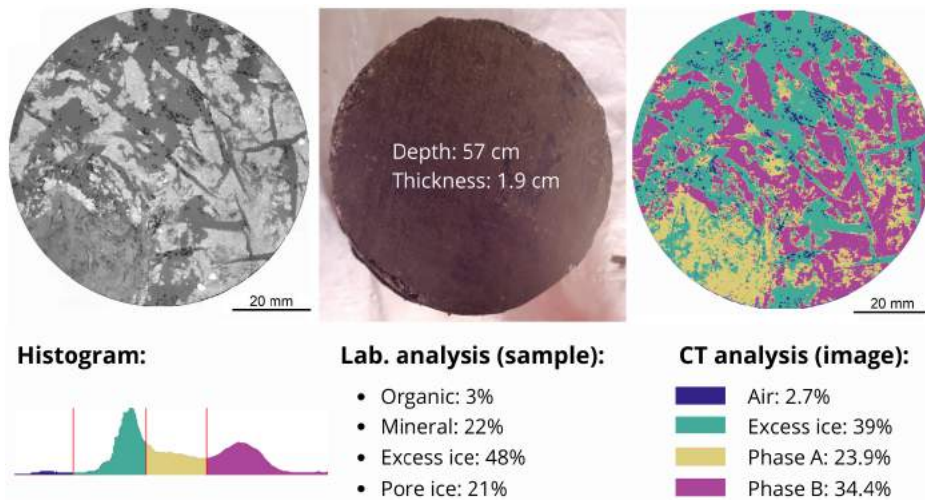
Figure 3.5: At a glance overview of manual thresholding segmentation of a CT image with brief analysis, histogram of the image, sample from laboratory which consists that CT image and laboratory analysis of that sample

The results of manual thresholding (Fig. 3.6) were visualized the same way as Fig. 3.2, within Python and Plotly library. Fig. 3.6 shows the result of classification with the manual thresholding method. This figure also displays results obtained by laboratory analyses for comparison. The length of each horizontal line represents the thickness of the permafrost core sample used to get the laboratory data.
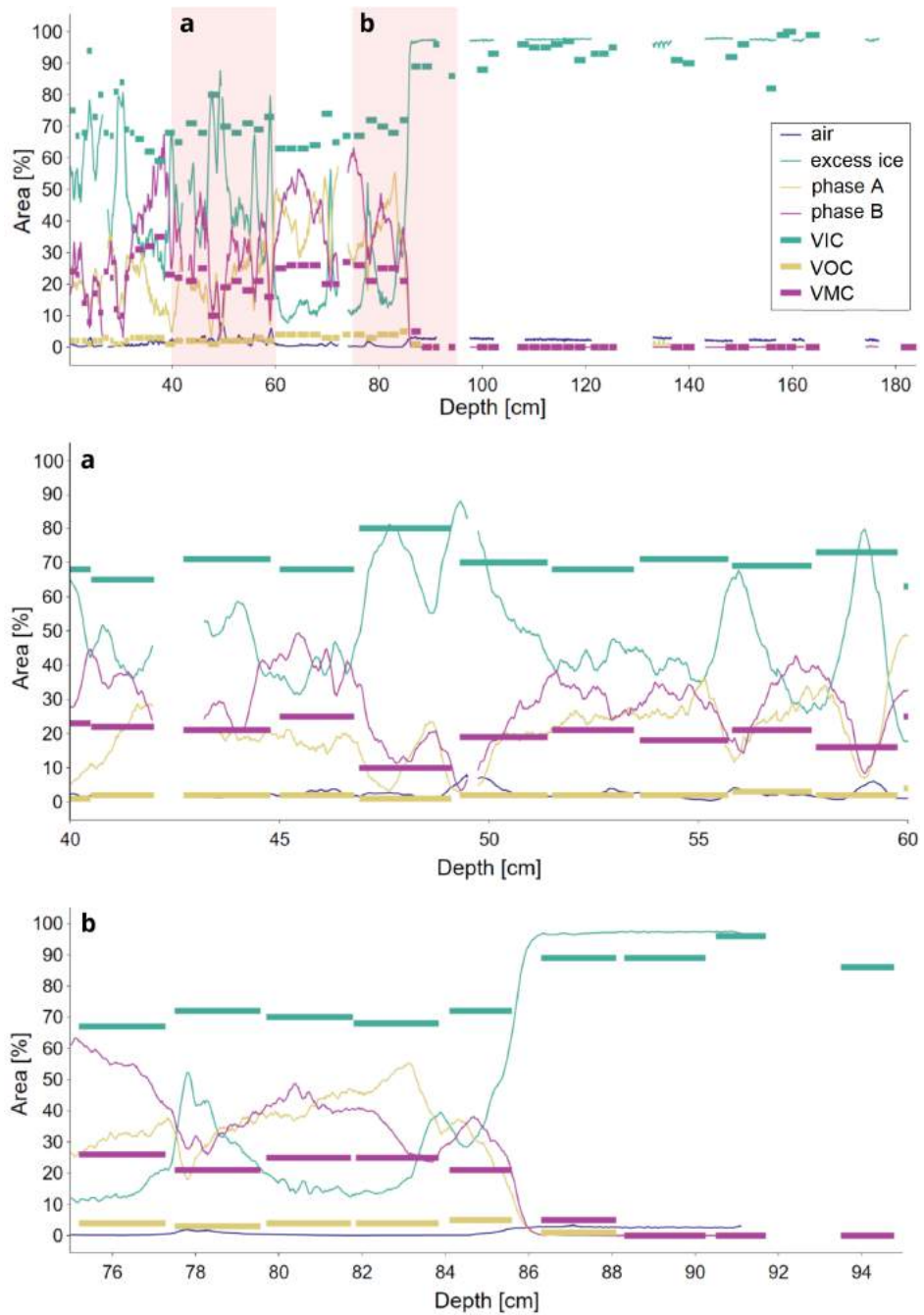
Figure 3.6: Compilation of segmentation results obtained by manual thresholding method and laboratory analyses method. With focuses on **(a)** 40-60 cm; **(b)** 75-95 cm. Laboratory derived data is visualised with horizontal line, where the length of the each horizontal line represents the depth and thickness of the corresponding permafrost core sample

Two areas of Fig. 3.6 are highlighted. The first area (Fig. 3.6a) was chosen because it demonstrates four well distinct ice peaks. Second (Fig. 3.6b) is the transition area between the upper part (20.3 - 86.4 cm, mix of air, ice, organic, mineral parts) and the bottom part (86.4 - 184.0 cm, mostly ice with a low fraction of air, with little or no fractions of organic and mineral parts). It should be noted that the laboratory data over ice peaks is flat. The manual thresholding technique allows to distinguish and measure air and excess ice with a high confidence level. However, comparing CT data and laboratory data has shown that this image processing method cannot detect pore ice fractions.

Summary of numerical results of manual thresholding for upper and lower parts of the core was combined in Table 3.1. According to mean values, through its length (20.3 - 86.4 cm), the upper core consists of three phases in almost equal proportions and a gas fraction of about one percent. The heterogeneous structure of the upper core can be observed through drastically various minimum and maximum values. Due to its homogeneous structure, the lower core demonstrates a different pattern, with min-mean-max values being relatively stable through the core. At the same time, a fraction of air has increased roughly to 2.5%.

Table 3.1: Ordinary least squares regression results

Volume [%]	CT scan (upper core)			CT scan (lower core)			CT scan (whole core)
	min	mean	max	min	mean	max	mean
Gas	0.01	1.21	7.92	1.70	2.44	3.46	1.70
Excess ice	7.55	37.41	93.05	93.15	97.34	98.28	61.45
Phase A	1.92	26.99	57.48	0.00	0.17	2.46	16.23
Phase B	2.50	34.38	67.52	0.00	0.03	2.44	20.61

Since the CT method could not display pore ice but could detect excess ice, it is of particular interest to compare CT excess ice with laboratory-measured excess ice values. Fig. 3.7 consists of three lines showing a compilation of excess and pore ice results. Excess ice obtained by CT is compared with excess ice and pore ice results derived through laboratory

data. Excess ice CT and lab, overall, have a high level of match. The sum of values of excess ice (lab) and pore ice (lab) is equal to VIC from Fig. 3.6.
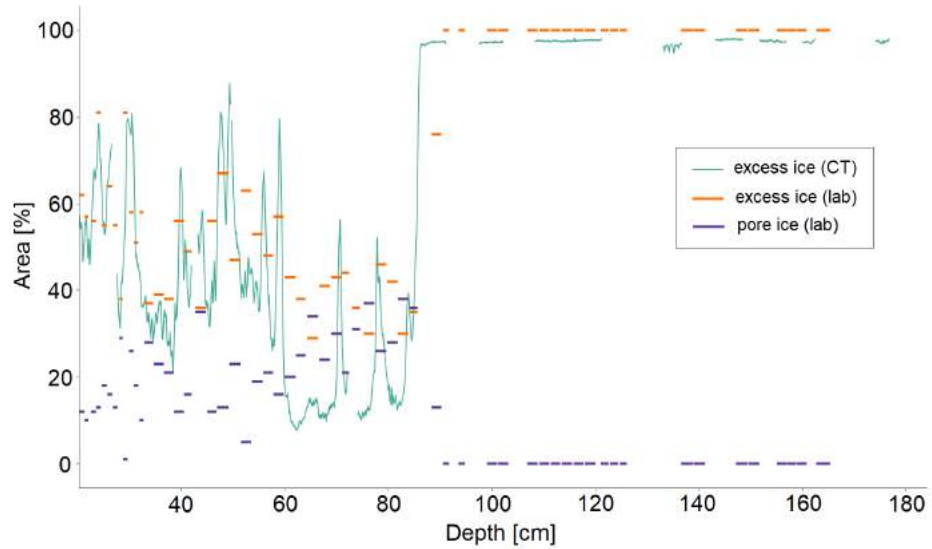
Figure 3.7: Excess ice CT segmentation result is depicted together with excess ice and pore ice results obtained through laboratory analyses

Fig. 3.8 shows high-resolution composition of the whole permafrost core. Fig. 3.8a is a compilation of field photos of the permafrost core analyzed in this thesis. Fig. 3.8b is CT scan as XZ plane compilation. Fig. 3.8c shows a compilation of segmented CT images and Fig. 3.8d shows an area graph with the area below the line filled in with a certain colour according to the constituent. Small gaps in Fig. 3.8a are caused by shortcomings during the sampling procedure. Bigger gaps in Fig. 3.8(b, c, d) are due to the fact that some parts of the have not been scanned by CT because they were either destroyed or too small to get an adequate result.
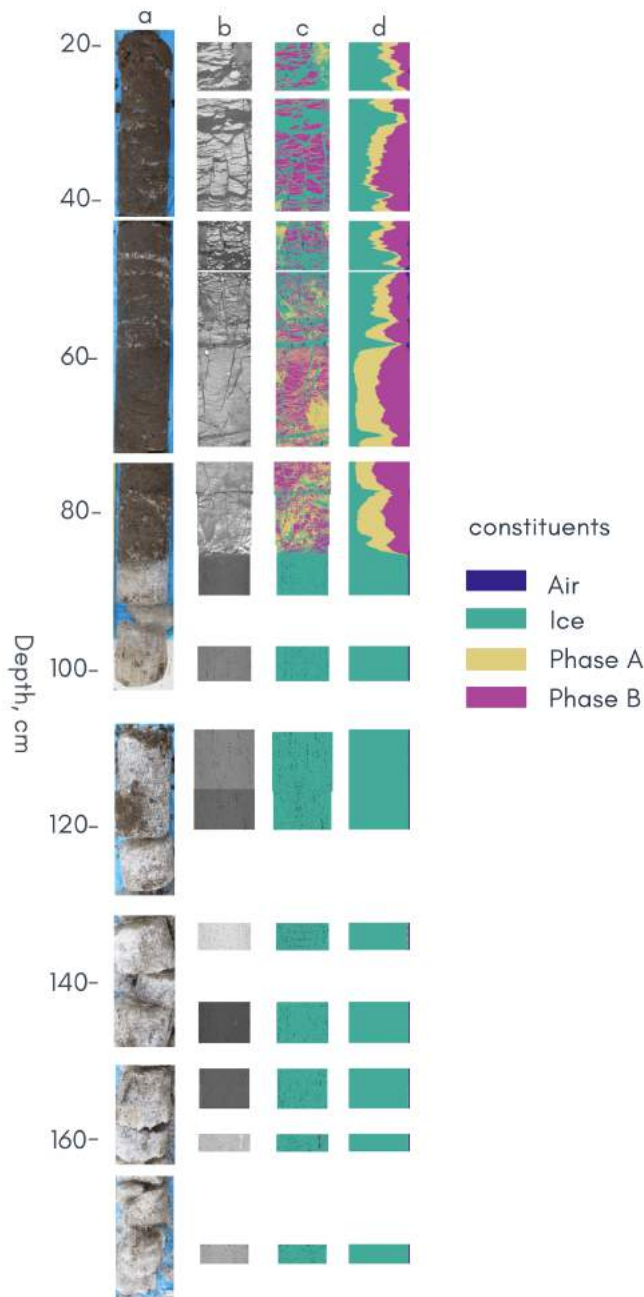
Figure 3.8: High resolution composition of the whole permafrost core analyzed in this thesis. **(a)** Photos of permafrost core; **(b)** CT scanning images (XZ plane); **(c)** Manual thresholding segmentation results; **(d)** Stacked area chart

Fig. 3.6 depicted drastic and abrupt change of constituents fractions between the upper part of the core and the bottom part of the core. The latter consists almost exclusively of excess ice and air. It is known that with increasing depth, the ice density increases due to settling and packing, while porosity is decreasing due to overburden pressure (Bender, 1997 [57]). Therefore, considering the relatively small depth, it is interesting to observe if the acquired result agrees with this expected trend. Fig. 3.9 shows correlations between gas and excess ice for the upper (Fig. 3.9a) and bottom (Fig. 3.9b) parts of the permafrost core. There is no significant correlation in the upper part of the core. Although, there is a strong correlation in the bottom part of the core. This happens since the bottom part of the core consists almost exclusively of air and ice. Therefore, if there is a bigger fraction of excess ice, there is less air and vice versa.
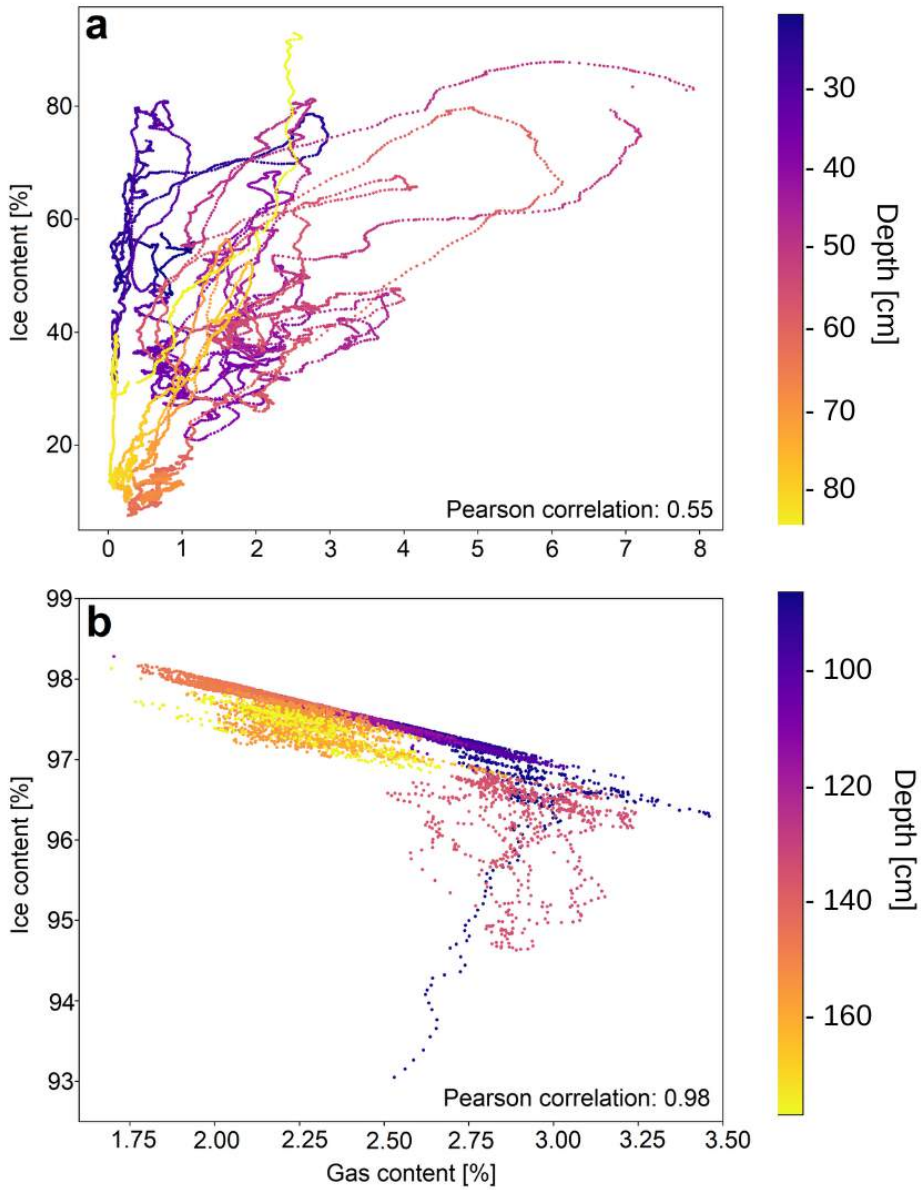
Figure 3.9: Correlation between excess ice and gas contents for **(a)** upper part of the core (20-86 cm) and **(b)** bottom part of the core (86-184 cm)

3.2 Statistical method

Apart from the CT method, a different approach to working with derived data has been implemented in this thesis. More precisely, a statistical modeling and regression analysis as a part of that modeling. The results of the regression analysis have been acquired through Python and Statsmodels module. That module provides functions for the computation of varying statistical models, tests, and data exploration. The regression analysis has been done with the ordinary least squares (OLS) method. OLS compares the difference between individual points in the data set and the predicted best fit line to measure the error produced. It is the most common method to estimate the linear regression equation. The summary of the model is depicted in Table 3.2.

Dep. Variable: y, stands for dependent variable. The dependent variable is laboratory measurements ($\theta_{i/o/m}$) and independent variables - CT images measurements ($\theta_{A/B/ei}$).

No. Observations: 159. This number has resulted as $53 \cdot 3$. In the laboratory, the permafrost core was cut into 66 samples. However, only 53 samples were used in regression analysis because some core parts were not scanned with a CT scanner. *Df Residuals: 155*, it is calculated as *No. Observations - number of predicting variables - 1.*

Covariance Type: nonrobust. It is a measure of how two variables are connected in a positive or negative manner. Robust covariance is calculated in such a way as to diminish or remove variables, which is not the case in this calculation.

R-squared: 0.945. It measures how much of the independent variable is explained by changes in our dependent variables. The result of 0.945 means that the model explains 94.5% of the change in the dependent variable. In theory, it is an excellent result, close to a perfect possible result, which is 1. However, a high R-squared value is not necessarily

good as a biased model can have a high R-squared value as well (Frost, 2019 [58]). The general opinion among statisticians, that there is no good R-squared score. Although, the acquired result, considering the field of science, is acceptable.

Adj. R-squared which stands for adjusted R-squared. It calculates R square only using variables whose addition to the model is significant. It also penalizes excessive use of variables and is always smaller than R-squared. The value of adjusted R-squared is more important than R-squared since my model contains more than one independent variable. However, since both numbers are very close, it can be concluded that all used independent variables are important and beneficial to the model.

Table 3.2: Ordinary least squares regression results

```
Dep. Variable:                    y   R-squared (uncentered):              0.945
Model:                          OLS   Adj. R-squared (uncentered):         0.943
Method:               Least Squares
Date:              Fri, 02 Jul 2021
Time:                      17:15:41
No. Observations:               159
Df Residuals:                   155
Df Model:                         4
Covariance Type:          nonrobust
==============================================================================
                 coef    std err          t      P>|t|      [0.025      0.975]
------------------------------------------------------------------------------
x1             0.1022      0.048      2.135      0.034       0.008       0.197
x2             0.2055      0.048      4.293      0.000       0.111       0.300
x3             0.0413      0.039      1.051      0.295      -0.036       0.119
x4             0.5218      0.039     13.270      0.000       0.444       0.599
```

The first column in the Table 3.2 is *coef* that stand for coefficients. It is the measurement of how a change in that variable affects the independent variable. There are no negative coefficients; therefore, there are no inverse relationships. As one rises, the other increases as well.

- $x_1 = \gamma_{A,o}$, the organic fraction of phase A
- $x_2 = \gamma_{A,m}$, the mineral fraction of phase A

- $x_3 = \gamma_{B,o}$, the organic fraction of phase B
- $x_4 = \gamma_{B,m}$, the mineral fraction of phase B

Once we obtain coefficient values (x_1, x_2, x_3, x_4) it is possible to calculate ice fractions for phase A and phase B as follows:

$$\gamma_{A,i} = 1 - \gamma_{A,o} + \gamma_{A,m} = 0.692 \tag{3.1}$$

$$\gamma_{B,i} = 1 - \gamma_{B,o} + \gamma_{B,m} = 0.436 \tag{3.2}$$

The result means that what was earlier identified as *organic phase* is 10.2% organic, 20.5% mineral, 69.2% ice. What earlier was identified as *mineral phase* is actually 4.1% organic, 52.1% mineral, 43.6% ice.

The second column in the Table 3.2 is *std err*, it is a probabilistic correction of the standard deviation (i.e., how dispersed the data is concerning the mean) of the coefficients that take into account the sample size. The results of standard deviation can be considered low, which means data are clustered around the mean.

The third column in the Table 3.2 is *t* which is a measurement with which precision the coefficient was measured. A low *std error* within a high *coefficient* produces a high *t-statistic*, which indicates a high significance for a certain coefficient. It is the case with the mineral fraction of phase B.

The fourth column in the Table 3.2 is $P > |\,t\,|$. It uses the *t-statistic* to produce the *p-value*, a measurement of how likely the coefficient is measured through the model by chance. The p-value of 0.295 for the organic fraction of phase B means a 29.5% chance that the organic fraction of phase B does not affect the dependent variable, and a result is produced by chance. Similarly, the *p-value* of the organic fraction of phase A is 3.4%. As for the mineral fraction of phase A and the mineral fraction of phase

B, the *p-value* is not equal to zero, as the *p-value* cannot be equal to zero. However, it is very close to zero, and it means that these results are significant. A coefficient considered statistically significant, if its *p-value* < 0.05.

At last, the fifth and sixth columns *[0.025 and 0.975]* are both measurements of values of coefficients within 95% of the data. Outside of these values can be considered outliers.

Fig. 3.10 shows the relationships between the predicted values and laboratory values, as well as R-squared values for each phase. R-squared is computed without centering (uncentered) since the model does not contain a constant. The regression model of the excess ice (Fig. 3.10a), accounts for 73% of the variance. For Phase B (Fig. 3.10b) the result is even higher - 89%. For Phase A (Fig. 3.10c) the R-squared result is relatively low - 22%.

Fig. 3.11 shows the results of regression analysis for predicted samples line (53 data-points), high-resolution line (31275 data-points), laboratory data, and CT images classification result. It can be noticed that the prediction sampling line and high-resolution prediction line are systematically higher than laboratory data. Although, both prediction lines and laboratory data are following the same trends. Also, the high resolution predicted line is always lower than the sampling prediction line whenever lines are going down. It happens due to the higher resolution of the first line. It is noticeable that two prediction lines and laboratory data are better aligned over the range of 20-60 cm, while the difference is more prominent in 60-90 cm. This may be due to different types of soil. Grain size distribution analysis could benefit in order to figure that out.

Each part of Fig. 3.11 consist of four lines:
- blue (**a** - VIC, **b** - VMC, **c** - VOC) - data obtained through laboratory analysis
- green (Predicted (samples)) - 53 data-points

- purple (High res predicted) - high resolution predicted, 31275 data-points
- red (**a** - Excess ice, **b** - Phase B, **c** - Phase A)) - data obtained through manual thresholding
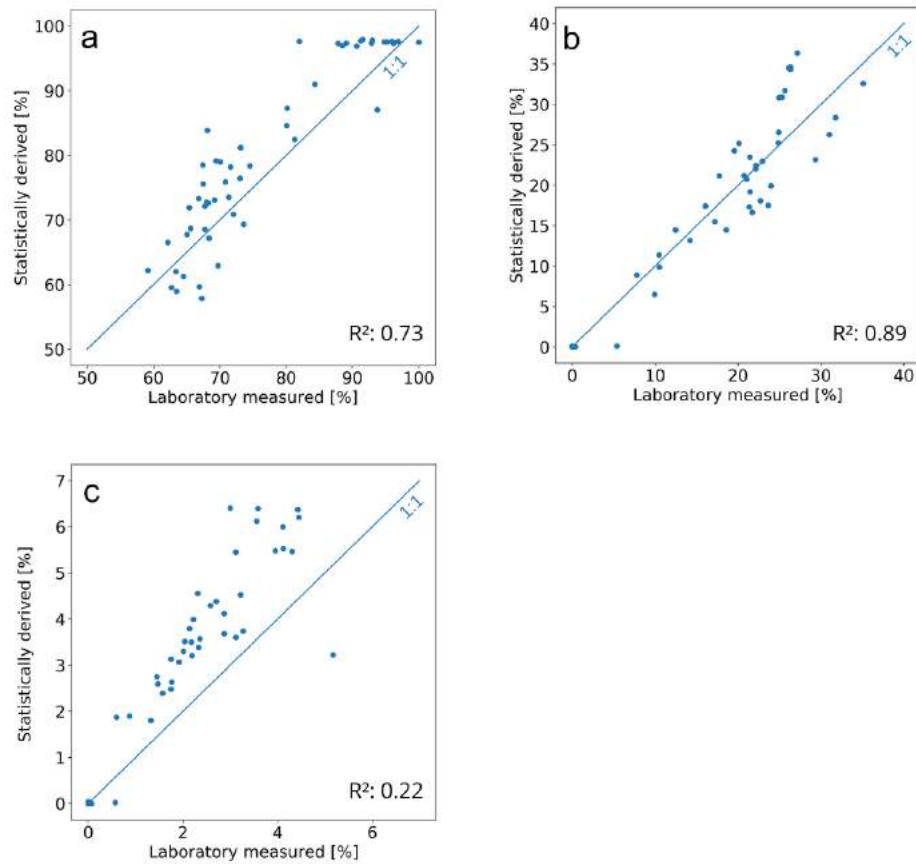
Figure 3.10: Relation between laboratory measured and statistically obtained values for the entire length of the core for sampled data **(a)** Excess ice; **(b)** Phase B; **(c)** Phase A
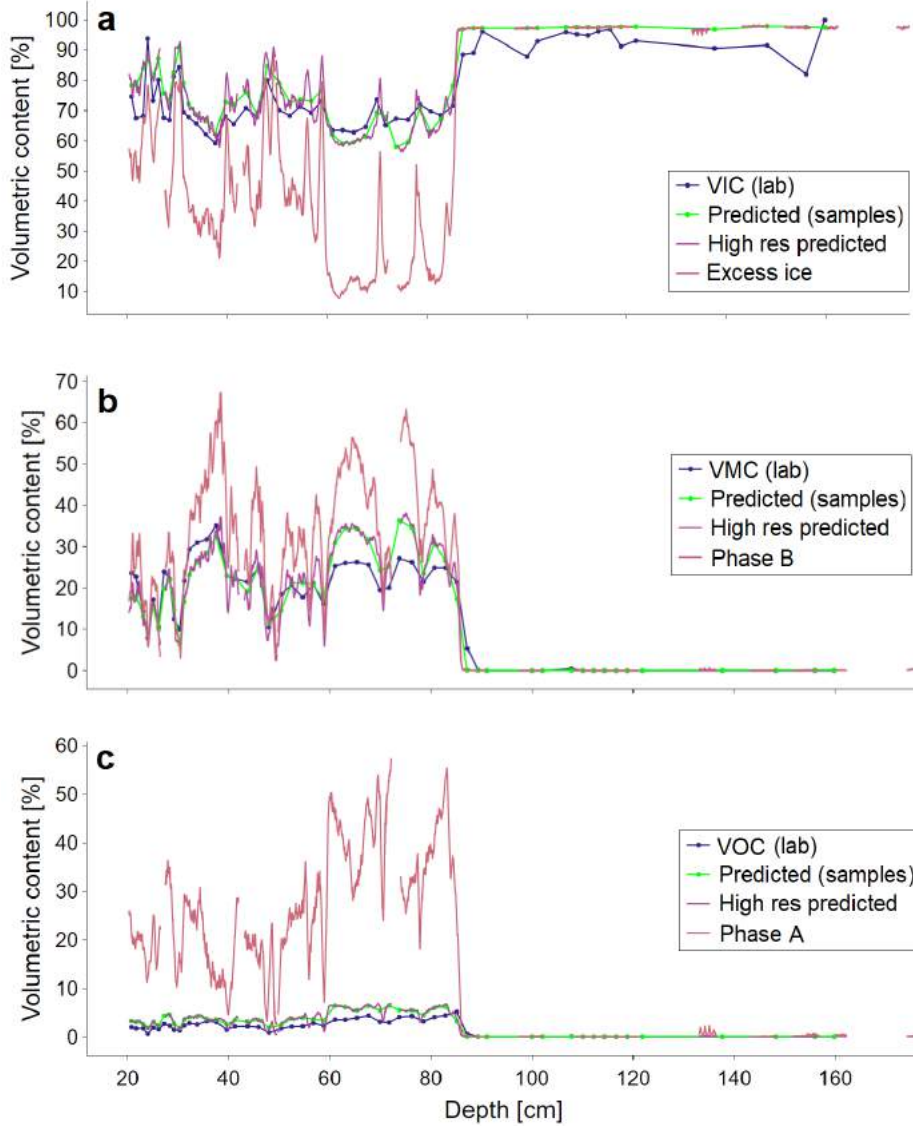
Figure 3.11: Compilation of laboratory-measured volumetric contents, statistically obtained results, high-resolution statistically obtained results and CT measured results over depth for **(a)** Excess ice; **(b)** Phase B; **(c)** Phase A. Y-scale is different for each of the subplot

Ultimately, since I obtained the results for the RA model, it is possible to calculate and merge it into a table for comparison. Table 3.3 shows mean, minimum and maximum values of results obtained within RA, both samples method and high-resolution method, as well as results derived through the laboratory analyses. Gas content values were acquired as subtraction of other contents from 100%.

Table 3.3: Calculated results of laboratory analysis, predicted (samples) and high resolution predicted values, summarising minimum (min), mean and maximum (max) values of IC, OC, and MC. Gas content values were acquired as subtraction of other contents from 100%

Volume [%]	Laboratory analysis			Predicted (samples)			High resolution predicted		
	min	mean	max	min	mean	max	min	mean	max
Ice content	59.19	76.89	100.00	62.00	80.24	97.50	56.20	81.69	98.28
Organic content	0.00	1.87	5.17	0.00	2.86	6.40	0.00	2.51	6.87
Mineral content	0.00	15.18	35.10	0.00	15.47	36.36	0.00	14.09	38.33
Gas content	-	6.06	-	-	1.43	-	-	1.71	-

4   Discussion

4.1 Estimation of physical properties of sediment core taken from Yedoma deposits in the Lena River delta in northern Siberia

Computed Tomography provides an efficient, relatively fast, and indestructible method of analysis of permafrost cores. It is especially efficient in dealing with large numbers of samples of permafrost core. Although, currently, the CT scanning method is still in a stage of development for soil science use (Iassonov, 2009 [56]). Estimation of volumetric contents of permafrost core assists in analyzing the structure and improves understanding of permafrost processes. Although, this operation requires a big effort at each step, starting with core sampling and ending with images analysis. The latter is especially challenging because the complicated structure of the images directly affects the segmentation procedure and complexifies it. Qualitative image segmentation is crucial for subsequent quantitative analysis of CT images (Iassonov, 2009 [56]). Different studies on permafrost cores and computed tomography deal with segmentation within varying thresholding techniques. These techniques, in turn, are always working with histograms. Using local spatial information within the manual thresholding method benefits the quality of segmentation results (Iassonov, 2009 [56]; Hagenmuller, 2013 [59]). However, there is always some subjectivity involved in choosing correct threshold values (Iassonov, 2009 [56]; Schlueter, 2010 [60]). Most studies focus on three main components - gas/air, ice, and sediment, both organic and inorganic (Calmels, 2010 [24]). In this thesis, after careful consideration

of segmentation results, a different approach towards four components of permafrost core was adopted - gas, excess ice, and two phases, each consisting of some fraction of pore ice, organic, and mineral components.

Gases in permafrost are of interest due to their potential contribution to enhanced climate warming. Previous studies (Calmels, 2010 [24]; Romanenko, 2017 [61]) have reported that it is possible to acquire accurate results in measuring gas content with CT. My experience can confirm that. Overall, I can state that segmentation of gas fraction is the most straightforward and most precise due to its low density and consequently dark color, which could be segmented surely. Ice content is another vital component as it may be used to determine ground settling induced by permafrost degradation (Calmels, 2010 [24]). However, currently, there are no landscape-scale studies of permafrost ground ice volumes using the CT. There are some ground ice content models (Couture, 2017 [62]) and some cryostratigraphy content models (Kanevskiy, 2014 [63]) but no vertical high resolution analyzed images that may be used for accurate detection of short-term changes. Segmentation of the ice part of the core is more challenging than the gas content but still significantly more straightforward than the other two fractions. Similar to Calmels (2004 [64]), who reported no significant correlation between gas and ice contents in the core, my results are in agreement. Fig. 3.9 shows no notable correlation in the upper part of the core. Pearson correlation of 0.55 proves that both contents are independent of each other. The importance of organic content is rising in parallel with climate change. Global warming in the Arctic and Yedoma region causes significant changes, including permafrost erosion and increased active layer thickness. These processes may affect OC releasing rates. Even though, general understanding of ground IC and OC release is improving (Tanski, 2021 [65] unpublished paper), there are still knowledge gaps regarding OC release rates and mechanisms on a landscape scale.

In this thesis, I did not intend to analyze cryostructures and cryotextures, however, it is another option for studying permafrost processes within

the CT method. Since classifying and identification of both cryotexture and cryostructure can explain the thermal history and origin of the substrate by which permafrost was formed and developed (Gilbert, 2016 [26]). Moreover, it would be almost impossible without CT to distinguish between different kinds of cryostructures (Calmels, 2008 [66]). Also, CT allows monitoring changes in configurations of air and ice in the course of various processes, as well as to carry out direct observations of different cryogenic processes in time (Romanenko, 2017 [61]).

4.2 CT and laboratory results comparison

Previous studies concluded that the CT method could estimate the ground-ice content of permafrost core (Delisle, 2003 [67]; Calmels, 2004 [64]). However, these studies did not correlate the CT results with laboratory results. In this thesis, I used CT scans of permafrost core and image processing algorithm for segmentation and quantification of permafrost core constituents. Laboratory data have been used only for comparison with CT results and as additional information for statistical analysis. It should also be noted that volume results are received directly within the CT scanning method, while for laboratory analyses, weight data was obtained first, and then the volume was calculated. The laboratory analyses were used for validation of CT results and estimation of possible errors.

I found out that the image processing technique adopted in this thesis provides segmentation results of permafrost core constituents with different confidence levels. The visualized comparison between CT and laboratory results (Fig. 3.6) shows that data derived from both methods overall demonstrate similar patterns but with different magnitudes. Moreover, CT scanning is the only method for direct determination of void and gas content in permafrost (Calmels, 2004 [64]). Comparing the segmentation results of ice fraction with laboratory-derived results has shown that the CT method can quantify only excess ice. One of the main reasons for that

is that the current CT scan resolution (50 μm) was insufficient to observe pore (interstitial) ice in the silty permafrost material. Other researchers also faced that problem (Calmels, 2004 [64]; Lapalme, 2017 [68]). Since pore ice is undetectable, CT analysis can directly measure excess ice but cannot measure total ice. Nevertheless, there is a potential for improved detection of VIC via the CT method, which primarily lies in different CT systems and higher pixel resolution (Lapalme, 2017 [68]).

The values of air quantified through the CT scanning method are ranging from almost zero to 7.9%, which is a maximum value in the upper part of the core (Table 3.1). The average gas content value for the upper core is 1.2%, and the bottom part is two times higher - 2.4%. Similar results were obtained by Calmels (2004 [64]) for a core located in discontinuous permafrost in northern Quebec with an average of 2.3% and values varying from 1% to 4%.

According to CT results (Table 3.1), the upper part of the core consists of excess ice and two fractions (phase A and phase B) in roughly equal proportions. However, the bottom part of the core is comprised almost entirely of ice - 97.3%.

Organic matter in the frozen ground often contains large pores filled with ice. Moreover, the voxels with values that fall within the ice density value or the other way around, some ice mixed with a large amount of peat can fall into the peat density value range. VOC value in Yedoma permafrost cores has been earlier evaluated by Windirsch (2020 [69]) and Wetterich (2020, [70]). Windirsch (2020 [69]) analyzed a 3 meters long Yedoma upland permafrost core from central Yakutia and reported a mean VOC value as 0.42% and a maximum of 1.4%. Wetterich (2020, [70]) analyzed two cryostratigraphic units: Unit A, dated from ca. 52 to 28 cal kyr BP and Unit B, dated from ca. 28 to 15 cal kyr BP. Both units are from Yedoma Ice Complex in the eastern Lena delta on Sobo-Sise Island. Wetterich (2020, [70]) reported VOC values for Unit A as 1.7%, 4.5%, and 15.1% for min, mean, and max, respectively. VOC values for Unit B were 0.5%, 2.1%, 5.1%

for min, mean, and max, respectively. I received similar VOC values for a plateau-situated permafrost core that was analyzed in this thesis. The results are depicted in the tables 3.1 (CT method) and 3.3 (laboratory and statistical methods).

4.3 Impact of different image processing approach and settings

The novelty of this thesis stems from the high spatial resolution (50 µm) of CT images. Compared with many previous studies, this resolution is higher than the spatial resolution used in some highly cited papers, such as (Schlueter, 2016 [71]) with 61 *µm* spatial resolution, (Calmels, 2004 [64]) - 100 *µm*, (Calmels, 2010 [24]) - 350 *µm*, (Lapalme, 2017 [68]) - 400 *µm*. The spatial resolution itself, for the most part, depends on the X-ray instrument used for scanning. Overall, it is possible to observe features such as ice lenses or gas bubbles already at the 100 *µm* scale (Calmels, 2010 [24]), but higher resolution allows to work with more detailed images. Resolution is one of the most critical characteristics of CT scanning that characterize the quality of the received images. There are three types of CT resolution, spatial, temporal, and contrast. In this thesis, the temporal resolution is of little importance since the imaged structure has no motion. The contrast resolution is not intrinsically high and inferior to MRI and PET (Lin, 2009 [72]). Finally, spatial resolution is of great importance because it defines the quality of the CT images and the ability to analyze and interpret the content. However, it should be noted that the scanning procedure depends not wholly on the resolution but it is also sensitive to varying scanning and reconstruction settings.

Segmentation was the most complicated part of this thesis. It resulted from the heterogeneous structure of the permafrost core and the uneven distribution of its constituents. The most complicated image stacks were the ones with two material densities close to each other or when

some constituents have sizes smaller than the spatial resolution of the CT system. My results have shown that manual thresholding performed significantly better than the automatic thresholding methods. Latter, in many cases, not only produced a less reliable result than manual but in several cases made apparent mistakes. Mostly these mistakes occurred between different image stacks. Another common problem in segmentation is noise and blur on CT images (Hagenmuller, 2016 [73]). However, in this work, this particular problem did not occur. In general, working with any kind of segmentation and with different thresholding techniques, there is always a problem of the absence of ground truth (Iassonov, 2009 [56], Hagenmuller 2013 [59]). It is impossible to know if the binarization result is optimal. The truth will always be, to some degree, within the eye of a researcher, and the final result will be affected by empirically collected information. Higher CT scanning resolution, prior knowledge of the core structure, features, and the intensity characteristics of the objects are beneficial.

With the development of CT technologies and its growing popularity, the question arises if CT can complement laboratory analysis or replace it. Despite the system's attenuation and throughput improvements, CT still has apparent limitations regarding segmentation uncertainties. Concerning limitations of the CT, any researcher working with CT images and deriving results through image analysis must remember that all images have been altered. Some CT image data is inevitably lost during the preprocessing phase. Moreover, some data is already lost or changed even before the scanning procedure as permafrost cores have been already altered. Because from the moment when the core has left the ground, it begins to deteriorate due to change in temperature (Calmels, 2004 [64]). It is also thawing partly and releasing included gases which may affect its phase composition. Another not obvious downside of the imaging approach is the time required to collect and process the data. However, this is comparable to the conventional laboratory method as the majority of time is spent allowing the sample to equilibrate (Tracy, 2014 [74]). It is, therefore, essential for researchers to direct efforts towards com-

bining CT with other complementary methods to enhance cutting-edge research while industrial work on improvement of the technology continues. (Mao, 2016 [75]). The result of Computed Tomography scanning can be enhanced in combination with other techniques. Previously, several researchers have already combined the CT method with other techniques for varying study objectives. Anderson (1989 [76]) and Metzner (2015 [77]) used a combination of CT and Magnetic resonance imaging (MRI). Arias (2010 [78]) and Hapca (2011 [79]) used CT and Scanning Electron Microscopy (SEM). Goethals (2009 [80]) used CT and Positron emission tomography (PET). In this thesis, I used a combination of CT scanning and linear regression analysis together with classical laboratory analysis. Even though the CT scanning method has demonstrated certain advantages over the classical method, it is still too early to obliterate the classical analysis. Moreover, the best results are usually achieved by combining CT with other complementary methods (Calmels, 2010 [24]; Hagenmuller, 2013 [59]; Mao, 2016 [75]). Improvements in speed, spatial resolution, and reconstruction time are expected within the next decade (Pelc, 2014 [81]).

Apart from the CT scanning method and laboratory analyses, I have also implemented a statistical approach. The idea for that appeared due to particular segmentation and detecting problems with the CT scanning method. Linear regression analysis revealed overall good correlations between laboratory-measured and statistically obtained values for Excess ice and Phase B (pure white color on CT images) with R-squared results of 0.73 and 0.89, respectively (Fig. 3.10). However, it also showed that Phase A underestimated measured VOC (R-squared is 0.22). The statistical method has shown promising results. However, there is room for improvement in regression analysis results. The results could be even more precise if samples were given different weights accordingly to their thickness. Also, in this case, it would be beneficial to use Weighted Least Squares (WLS) instead of OLS.

It is important to mention a significant application that has not been

addressed in the thesis - Deep Learning (DL). This method is considered to be more advanced and outperformed classical machine learning models and signal processing approaches (Bengio, 2013 [82]). IN DL, each pixel gets a label, and pixels with the same label are connected in regards to some visual or semantic property. Nowadays, image segmentation models that are based on DL often become the most precise through popular benchmarks (e.g., *ScanNet Benchmark*, *Berkeley Segmentation Benchmark*). Another advantage of DL is that it can deal with nonlinearities, unlike the regression method dealing with linear dependencies. Therefore, if the data have nonlinear dependencies, neural networks should perform better than regression. However, the RA also has several particular vital advantages in comparison with DL. Within R-squared/adjusted R-squared, it is possible to comprehend the strength of relationships between variables and see how much of the total variability in the data is explained by the model. Also, RA allows seeing which features are statistically significant and which are not. RA is more straightforward, versatile and allows to have a comparison between different models.

5 Conclusions

This thesis aims to estimate the volumetric content of a Yedoma permafrost core. By performing image analysis of CT images of a permafrost core, this thesis shows that computerized X-ray tomography for the segmentation of permafrost constituents is able to provide a result comparable with sample-destructive laboratory analysis. The obtained segmentation results clearly illustrate the benefits of working with high-resolution CT imagery and show the limitations that may still occur with such detailed images. An additional deficiency of this thesis can be attributed to the image processing algorithm. As the used algorithm was a compilation of different methods and no readily available algorithm was adopted entirely. Despite the popularity of the CT method in soil science, there is still no standard workflow model for working with soil images. Different researchers use varying image processing techniques and software (ImageJ, VGSTUDIO MAX, Avizo, PORE3D, MORPHO+, and others), having different configurations and effectiveness in quantitative, qualitative, and statistical data analysis. Moreover, new techniques and software are being produced. That means CT scanning most likely will continue to develop in the near future and may find further applications and techniques due to the constant development of the scanning systems. Another limitation of that work is that only one permafrost core has been analyzed. Thus no comparison is possible between different cores. Notwithstanding these limitations, this thesis contributes to reducing the research gap of Yedoma permafrost structure, thaw process, and organic content.

Yedoma permafrost is rapidly changing, and Arctic permafrost is changing along with it. This region is thawing faster than other parts of the world due to the impacts of increasing global warming and expanding human activity. Climate change is a common topic for mass media, and its impor-

tance and influence cannot be overestimated. In 2021, changing climate is a reason for thousands of young people to protest in the streets and demand action. One of the ongoing campaigns is "FightFor1Point5", showing that these minors are already familiar with an IPCC special report regarding the impacts of global warming of 1.5 °C above pre-industrial levels at such a young age. However, even with all this attention, there are still gaps in our knowledge regarding permafrost thaw and degradation on the pan-Arctic scale. At the moment, articles and reports are appealing to researchers from various disciplines to unite to investigate the processes, timespan, and consequences of permafrost thaw to the global climate to avert a possible disaster. Focus areas of future researches that are designed to improve our understanding may include ground ice content characteristics, organic content emissions, extended modeling of permafrost carbon feedbacks, and evaluation of the vulnerability of organic carbon pools in the Earth system.

The possibly boundless life expectancy of CT information makes them valuable to the researchers who made the beginning check and future analysts who may inquire questions that the initial researcher would never have considered. Therefore, an appropriate and convenient way of storing, sharing, and licensing CT information and datasets would benefit future researchers.

Bibliography

[1] Harris S.; French H.; Heginbottom J.; Johnston G.; Ladanyi B.; Sego D.; van Everdingen R. **Glossary of Permafrost and Related Ground-Ice Terms**. *National Research Council Canada* (1988) (see page 1).

[2] Obu J. **How Much of the Earth's Surface is Underlain by Permafrost?** *Journal of Geophysical Research: Earth Surface* 126 (1988). DOI: 10.1029/2021JF006123 (see page 1).

[3] Tarnocai C.; Canadell J.; Schuur E.; Kuhry P.; Mazhitova G.; Zimov S. **Soil organic carbon pools in the northern circumpolar permafrost region**. *Global Biogeochemical Cycles* 23 (2009). DOI: 10.1029/2008GB003327 (see pages 1, 2).

[4] Hugelius G.; Strauss J.; Zubrzycki S.; Harden J.; Schuur E.; Ping C.; Schirrmeister L.; Grosse G.; Michaelson G.; Koven C.; O'Donnell J.; Elberling B.; Mishra U.; Camill P.; Yu Z.; Palmtag J. and Kuhry P. **Estimated stocks of circumpolar permafrost carbon with quantified uncertainty ranges and identified data gaps**. *Biogeosciences* 11 (2014), 6573–6593. DOI: 10.5194/bg-11-6573-2014 (see page 1).

[5] Poertner H.; Roberts D.; Masson-Delmotte V.; Zhai P.; Tignor M.; Poloczanska E.; Mintenbeck K.; Alegría A.; Nicolai M.; Okem A.; Petzold J.; Rama B.; Weyer N. **IPCC Special Report on the Ocean and Cryosphere in a Changing Climate**. *Intergovernmental Panel on Climate Change* (2019) (see page 1).

[6] Richter-Menge J.; Overland J. **Arctic Report Card** (2009). URL: arctic.noaa.gov/reportcard (see page 1).

[7] Schaedel C.; Bader M.; Schuur E.; Biasi C.; Bracho R.; Capek P.; De Baets S.; Diakova K.; Ernakovich J.; Estop-Aragones C.; Graham D.; Hartley I.; Iversen C.; Kane E.; Knoblauch C.; Lupascu M.; Martikainen P.; Natali S.; Norby R.; O'Donnell J.; Chowdhury T.; Santruckova H.; Shaver G.; Sloan V.; Treat C.; Turetsky M.; Waldrop M. and Wickland K. **Potential carbon**

emissions dominated by carbon dioxide from thawed permafrost soils. *Nature Climate Change* 6 (2016), 950–953. DOI: 10.1038/nclimate3054 (see page 1).

[8]   Boike J.; Langer M.; Lantuit H.; Muster S.; Roth K.; Sachs T.; Overduin P.; Westermann S. and McGuire D. **Permafrost–physical aspects, carbon cycling, databases and uncertainties**. *Recarbonization of the Biosphere: Ecosystems and the Global Carbon Cycle* (2012), 159–185. DOI: 10.1007/978-94-007-4159-1_8 (see pages 1, 2).

[9]   Schneider von Deimling T.; Lee H.; Ingeman-Nielsen T.; Westermann S.; Romanovsky V.; Lamoureux S.; Walker D.; Chadburn S.; Trochim E.; Cai L.; Nitzbon J.; Jacobi S. and Langer M. **Consequences of permafrost degradation for Arctic infrastructure – bridging the model gap between regional and engineering scales**. *The Cryosphere*: 15 (2021), 2451–2471. DOI: 10.5194/tc-15-2451-2021 (see page 1).

[10]   Huissteden J. **Thawing Permafrost**. Gewerbestrasse 11, 6330 Cham, Switzerland: Springer Nature Switzerland AG, 2020 (see page 2).

[11]   Schirrmeister L.; Grosse G.; Wetterich S. Overduin P.; Strauss J.; Schuur E. and Hubberten H. **Fossil organic matter characteristics in permafrost deposits of the northeast Siberian Arctic**. *Journal of Geophysical Research* 116 (2011). DOI: 10.1029/2011JG001647 (see page 2).

[12]   Zimov S.; Voropaev Y.; Semiletov I.; Davidov S.; Prosiannikov S.; Chapin F.; Chapin M.; Trumbore S.; Tyler S. **North Siberian Lakes: A Methane Source Fueled by Pleistocene Carbon**. *Science* 277:800 (1997). DOI: 10.1126/science.277.5327.800 (see page 2).

[13]   Grosse G.; Robinson J.; Bryant R.; Taylor M.; Harper W.; DeMasi A.; Kyker-Snowman E.; Veremeeva A.; Schirrmeister L. and Harden J. **Distribution of late Pleistocene ice-rich syngenetic permafrost of the Yedoma Suite in east and central Siberia, Russia**. Tech. rep. 2013-1078. 12201 Sunrise Valley Reston, VA 20192: United States Geological Survey, 2013 (see page 2).

[14]   Morgenstern A.; Grosse G.; Gunther F.; Fedorova I. and Schirrmeister L. **Spatial analyses of thermokarst lakes and basins in Yedoma landscapes of the Lena Delta**. *Annals of the Association of American Geographers* 5 (2011), 1495–1545. DOI: 10.5194/tcd-5-1495-2011 (see page 2).

[15] Schuur E.; Abbott B.; Bowden W.; Brovkin V.; Camill P.; Canadell J.; Chanton J.; Chapin F.; Christensen T.; Ciais P.; Crosby B.; Czimczik C.; Grosse G.; Harden J.; Hayes D.; Hugelius G.; Jastrow J.; Jones J.; Kleinen T.; Koven C.; Krinner G.; Kuhry P.; Lawrence D.; McGuire A.; Natali S.; O'Donnell J.; Ping C.; Riley W.; Rinke A.; Romanovsky V.; Sannel A.; Schädel C.; Schaefer K.; Sky J.; Subin Z.; Tarnocai C.; Turetsky M.; Waldrop M.; Walter A.; Wickland K.; Wilson C.; Zimov S. **Expert assessment of vulnerability of permafrost carbon to climate change**. *Climatic Change* 119 (2013), 359–374. DOI: 10.1007/s10584-013-0730-7 (see page 2).

[16] Turetsky M.; Abbott B.; Jones M.; Walter A.; Olefeldt D.; Schuur E.; Koven C.; McGuire D.; Grosse G.; Kuhry P.; Hugelius G.; Lawrence D.; Gibson C. and Sannel B. **Permafrost collapse is accelerating carbon release**. *Nature* 569:7754 (2019), 32–34. DOI: 10.1038/d41586-019-01313-4 (see page 2).

[17] Rowland J.; Jones C.; Altmann G.; Bryan R.; Crosby B.; Geernaert G.; Hinzman L.; Kane D.; Lawrence D.; Mancino A.; Marsh P.; McNamara J.; Romanovsky V.; Toniolo H.; Travis B.; Trochim E. and Wilson C. **Arctic Landscapes in Transition: Responses to Thawing Permafrost**. *Eos, Transactions, American Geophysical Union* 91:26 (2010), 229–236. DOI: 10.1029/2010EO260001 (see page 2).

[18] Siewert M.; Lantuit H.; Richter A. and Hugelius G. **Permafrost Causes Unique Fine-Scale Spatial Variability Across Tundra Soils**. *Global Biogeochemical Cycles* 35 (2021). DOI: 10.1029/2020GB006659 (see page 2).

[19] Lee H.; Swenson S.; Slater A. and Lawrence D. **Effects of excess ground ice on projections of permafrost in a warming climate**. *Environ. Res. Lett.* 9 (2014). DOI: 10.1088/1748-9326/9/12/124006 (see page 4).

[20] Mackay R. **The world of underground ice**. *Annals of the Association of American Geographers* 62:1 (1972), 1–22. DOI: 10.1111/j.1467-8306.1972.tb00839.x (see page 4).

[21] Calmels F.; Gagnon O. and Allard M. **A Portable Earth-drill System for Permafrost Studies**. *Permafrost and Periglac. Process.* 16 (2016), 311–315. DOI: 10.1002/ppp.529 (see page 4).

[22] Zubrzyscki S. **Drilling Frozen Soils in Siberia**. *Polarforschung* 81:2 (2011), 150–152 (see page 4).

[23] Van Geet M. Mees F. Swennen R. and Jacobs P. **Applications of X-ray computed tomography in the geosciences**. *Geological Society* 215 (2003), 1–6. DOI: 10.1144/GSL.SP.2003.215 (see page 5).

[24] Calmels F.; Clavano W. and Froese D. **Progress on X-ray computed tomography (CT) scanning in permafrost studies**. In: Geo2010; in the new West; 2010 Calgary conference. Vancouver, BC, Canada: Canadian Geotechnical Conference, 2010, 1353–1358 (see pages 5, 51, 52, 55, 57).

[25] Cnudde V.; Boone M. **High-resolution X-ray computed tomography in geosciences: A review of the current technology and applications**. *Earth-Science Reviews* 123 (2013), 1–17. DOI: 10.1016/j.earscirev.2013.04.003 (see page 5).

[26] Gilbert G.; Kanevskiy M. and Murton J. **Organic carbon in ice-rich permafrost: Characteristics, quantity, and availability**. *Permafrost and Periglac. Process.* 27 (2016), 377–389. DOI: 10.1002/ppp.1912 (see pages 5, 53).

[27] Katasonov E. **Lithology of frozen Quaternary deposits (cryolithology) of the Yana Coastal Plain**. PhD thesis. Obruchev Permafrost Institute, 1954 (see page 5).

[28] Murton J. **Ground ice and cryostratigraphy**. *Treatise on Geomorphology* 8 (2013), 173–201. DOI: 10.1016/B978-0-12-374739-6.00206-2 (see page 5).

[29] Yu L.; Vrieze T.; Leng S.; Fletcher J. and McCollough C. **Technical Note: Measuring contrast- and noise-dependent spatial resolution of an iterative reconstruction method in CT using ensemble averaging**. *Radiation imaging physics* (2016). DOI: 10.1118/1.4916802 (see page 9).

[30] Tan M.; Chin N.; Yusof Y.; Abdullah J. **Novel 2D and 3D imaging of internal aerated structure of ultrasonically treated foams and cakes using X-ray tomography and X-ray microtomography**. *Journal of Food Engineering* 183 (2016), 9–15 (see page 9).

[31] Mukhopadhyay S.; Masto R.; Tripathi R. and Srivastava N. **Application of Soil Quality Indicators for the Phytorestoration of Mine Spoil Dumps**. Dhanbad, India: Industrial Biotechnology, Waste Utilization Research Group, CSIR-Central Institute of Mining, and Fuel Research, 2019 (see page 13).

[32] Froeb K. **Measuring and modeling of soil thermal properties and ground heat flux at two different sites at Lena Delta, Siberia**. MA thesis. Augustuspl. 10, 04109 Leipzig: Universitaet Leipzig, 2011 (see page 13).

[33] Mollaret C.; Wagner F.; Hilbich C.; Scapozza C. and Hauck C. **Petrophysical Joint Inversion Applied to Alpine Permafrost Field Sites to Image Subsurface Ice, Water, Air, and Rock Contents**. *Front. Earth Sci.* 8:85 (2020). DOI: 10.3389/feart.2020.00085 (see page 14).

[34] Voitkovskii K. **The mechanical properties of ice**. *Izd. Akademii Nauk SSSR* (1960) (see pages 15, 20).

[35] Strauss J. **Organic carbon in ice-rich permafrost: Characteristics, quantity, and availability**. PhD thesis. Telegrafenberg, Gebaeude A45, 14473 Potsdam: Alfred Wegener Institute Helmholtz Centre for Polar and Marine Research, Sept. 2014 (see page 15).

[36] Monhonval A.; Mauclet E.; Pereira B.; Vandeuren A.; Strauss J.; Grosse G.; Schirrmeister L.; Fuchs M.; Kuhry P. and Opfergelt S. **Mineral Element Stocks in the Yedoma Domain: A Novel Method Applied to Ice-Rich Permafrost Regions**. *Front. Earth Sci.* 9 (2021). DOI: 10.3389/feart.2021.703304 (see page 16).

[37] Monhonval A.; Mauclet E.; Pereira B.; Vandeuren A.; Strauss J.; Grosse G.; Schirrmeister L.; Fuchs M.; Kuhry P. and Opfergelt S. **The next generation of climate model should account for the evolution of mineral-organic interactions with permafrost thaw**. *Environ. Res. Lett.* 15 (2020). DOI: 10.1088/1748-9326/ab9a6d (see page 16).

[38] Chaki J and Dey N. **A Beginner's Guide to Image Preprocessing Techniques**. Boca Rator, FK 33487-2742: Taylor and Francis Group, LLC, 2019 (see page 17).

[39] Schindelin J.; Arganda-Carreras I.; Frise E.; Kaynig V.; Longair M.; Pietzsch T.; Preibisch S.; Rueden C.; Saalfeld S.; Schmid B.; Tinevez J.; White D.; Hartenstein V.; Eliceiri K.; Tomancak P. and Cardona A. **Fiji: an open-source platform for biological-image analysis**. *Nature methods* 9 (2012), 676–682. DOI: 10.1038/nmeth.2019 (see page 17).

[40] Yuheng S. and Hao Y. **Image Segmentation Algorithms Overview**. *ArXiv website* (2017). DOI: 1707.02051 (see page 20).

[41] Talay T. **Introduction to the Aerodynamics of Flight**. *NASA SP-367, National Aueronautics and Space Administration* (1975), 6–9 (see page 20).

[42] Meijboom F.; Hassink J. and van Noordwijk M. **Density fractionation of soil macroorganic matter using silica suspensions**. *Soil Biol. Biorchem.* 27:8 (1995), 1109–1111. DOI: 0038-0717(95)00028-3 (see page 20).

[43] De Vries H.; De Jager C. and De Vries C. **Nuclear charge-density-distribution parameters from elastic electron scattering**. *Atomic data and nuclear data tables* 36 (1987), 495–536 (see page 20).

[44] Salem S.; Kalyankar N. and Khamitkar S. **Image Segmentation by Using Thershold Techniques**. *Journal of Computing* 2:5 (2010) (see page 21).

[45] Otsu N. **A thresholding selection method from gray-level histograms**. *IEEE Trans System Man Cybernetic* 9 (1979), 62–66 (see page 22).

[46] Bangare S.; Dubal A.; Bangare P.; Patil S. **Reviewing Otsu's Method For Image Thresholding**. *International Journal of Applied Engineering Research* 10:9 (2015), 21777–21783 (see page 22).

[47] MacQueen J. **Some methods for classification and analysis of multivariate observations**. *Berkeley Symposium on Mathematical Statistics and Probability* (1967), 281–297 (see page 23).

[48] Liu D. and Yu J. **Otsu Method and K-means**. *Ninth International Conference on Hybrid Intelligent Systems* (2019), 344–349. DOI: 10.1109/HIS. 2009.74 (see page 23).

[49] Dhanachandra N.; Manglem K. and Chanu Y. **Image Segmentation using K-means Clustering Algorithm and Subtractive Clustering Algorithm**. *Procedia Computer Science* 54 (2015), 764–771. DOI: 10.1016/j. procs.2015.06.090 (see page 24).

[50] Kittler J. and Illingworth J. **Minimum Error Thresholding**. *Pattern Recognition* 19:1 (1986), 41–47 (see page 24).

[51] O'Gorman L.; Sammon M.; Seul M. **Practical algorithms for image analysis**. Cambridge, New York: Cambridge University Press, 2018 (see pages 24, 25).

[52] Azhar H.; Widjanarko T. **Comparison of Two Binary Image Thresholding Methods**. *Random Signal Analysis* (2002) (see page 25).

[53] Kluyver T.; Ragan-Kelley B.; Perez F.; Granger B.; Bussonnier M.; Frederic J.; Kelley K.; Hamrick J.; Grout J.; Corlay S.; Ivanov P.; Avila D.; Abdalla S. and Willing C. **Jupyter Notebooks – a publishing format for reproducible computational workflows**. *Positioning and Power in Academic Publishing* (2016), 87–90. DOI: 10.3233/978-1-61499-649-1-87 (see page 29).

[54] Bradski G. and Kaehler A. **Learning OpenCV**. 1005 Gravenstein Highway North, Sebastopol, CA 95472: O'Reilly Media Inc., 2008 (see page 33).

[55] Perkel J. **Data visualization tools drive interactivity and reproducibility in online publishing**. *Nature Briefing* 554 (2018), 133–134. DOI: 10.1038/d41586-018-01322-9 (see page 33).

[56] Iassonov P.; Gebrenegus T. and Tuller M. **Segmentation of X-ray computed tomography images of porous materials: A crucial step for characterization and quantitative analysis of pore structures**. *Water resources research* 45 (2009). DOI: 10.1029/2009WR008087 (see pages 35, 51, 56).

[57] Bender M.; Sowers T. and Brook E. **Gases in ice cores**. *Proc. Natl. Acad. Sci. USA* 94 (1997), 8343–8349. DOI: 10.1073/pnas.94.16.8343 (see page 42).

[58] Frost J. **Introduction to Statistics: An Intuitive Guide for Analyzing Data and Unlocking Discoveries**. State College, PA 16801: Statistics by Jim Publishing, 2019 (see page 45).

[59] Hagenmuller P.; Chambon G.; Lesaffre B.; Flin F.; Naaim M. **Energy-based binary segmentation of snow microtomographic images**. *Journal of Glaciology* 59:217 (2013), 859–873. DOI: 10.3189/2013JoG13J035 (see pages 51, 56, 57).

[60] Schlueter S.; Weller U.; Vogel H. **Segmentation of X-ray micro tomography images of soil using gradient masks**. *Computers & Geosciences* 36 (2010), 1246–1251. DOI: 10.1016/j.cageo.2010.02.007 (see page 51).

[61] Romanenko K.; Abrosimov K.; Kurchatova A.; Rogov V. **The experience of applying X-ray computer tomography to the study of microstructure of frozen ground and soils**. *Earth's Cryosphere* 21:4 (2017), 75–81. DOI: 10.21782/KZ1560-7496-2017-4(75-81) (see pages 52, 53).

[62] Couture N. and Pollard W. **A Model for Quantifying Ground-Ice Volume, Yukon Coast, Western Arctic Canada**. *Permafrost and Periglac. Process.* 28 (2017), 534–542. DOI: 10.1002/ppp.1952 (see page 52).

[63] Kanevskiy M.; Jorgenson T.; Shur Y.; O'Donnell J.; Harden J.; Zhuange Q. and Fortiera D. **Cryostratigraphy and Permafrost Evolution in the Lacustrine Lowlands of West-Central Alaska**. *Permafrost and Periglac. Process.* 25 (2014), 14–34. DOI: 10.1002/ppp.1800 (see page 52).

[64] Calmels F. and Allard M. **Ice Segregation and Gas Distribution in Permafrost using Tomodensitometric Analysis**. *Permafrost and Periglac. Process.* 15 (2004), 367–378. DOI: 10.1002/ppp.508 (see pages 52–56).

[65] Tanski G.; Pika P.; Eisses B.; Calmels F.; Roy L.; Speetjens N.;Koch B.; Knoblauch C.; Bröder L.; Lantuit H.; Hugelius G.; Wolter J.; Richter A.; Fortier D.; Paquette M.; Fritz M. and Vonk J. **Landscape-related ground ice variability on the Yukon coastal plain inferred from computed tomography and potential implications on lateral permafrost carbon release**. 2021 (see page 52).

[66] Calmels F.; Allard M. **Segregated Ice Structures in Various Heaved Permafrost Landforms Through CT Scan**. *Earth Surface Processes and Landforms* 33 (2008), 209–225. DOI: 10.1002/esp.1538 (see page 53).

[67] Delisle G.; Allard M.; Fortier R.; Calmels F. and Larrive E. **Umiujaq, Northern Que´bec: Innovative Techniques to Monitor the Decay of a Lithalsa in Response to Climate Change**. *Permafrost and Periglac. Process.* 14 (2003), 375–385. DOI: 10.1002/ppp.469 (see page 53).

[68] Lapalme C.; Lacelle D.; Pollard W.; Fortier D.; Davila A. and McKay C. **Cryostratigraphy and the Sublimation Unconformity in Permafrost from an Ultraxerous Environment, University Valley, McMurdo Dry Valleys of Antarctica**. *Permafrost and Periglac. Process.* 28 (2017), 649–662. DOI: 10.1002/ppp.1948 (see pages 54, 55).

[69] Windirsch T.; Grosse G.; Ulrich M.; Schirrmeister L.; Fedorov A.; Konstantinov P.; Fuchs M.; Jongejans L.; Wolter J.; Opel T. and Strauss J. **Organic carbon characteristics in ice-rich permafrost in alas and Yedoma deposits, central Yakutia, Siberia**. *Biogeosciences* 17 (2020), 3797–3814. DOI: 10.5194/bg-17-3797-2020 (see page 54).

[70] Wetterich S.; Kizyakov A.; Fritz M.; Wolter J.; Mollenhauer G.; Meyer H.; Fuchs M.; Aksenov A.; Matthes H.; Schirrmeister L. and Opel T. **The cryostratigraphy of the Yedoma cliff of Sobo-Sise Island (Lena delta) reveals permafrost dynamics in the central Laptev Sea coastal**

region during the last 52 kyr. *The Cryosphere* 14 (2020), 4524–4551. DOI: 10.5194/tc-14-4525-2020 (see page 54).

[71] Schlüter S.; Leuther F.; Vogler S. and Vogel H. **X-ray microtomography analysis of soil structure deformation caused by centrifugation**. *Solid Earth* 7 (2016), 129–140. DOI: 10.5194/se-7-129-2016 (see page 55).

[72] Lin E.; Alessio A. **What are the basic concepts of temporal, contrast, and spatial resolution in cardiac CT?** *J Cardiovasc Comput Tomogr.* 3:6 (2009), 403–408. DOI: 10.1016/j.jcct.2009.07.003 (see page 55).

[73] Hagenmuller P.; Matzl M.; Chambon G. and Schneebeli M. **Sensitivity of snow density and specific surface area measured by microtomography to different image processing algorithms**. *The Cryosphere Discuss.* (2016). DOI: 10.5194/tc-2015-217 (see page 56).

[74] Tracy S.; Daly K.; Sturrock C.; Crout N.; Mooney S. and Roose T. **Three-dimensional quantification of soil hydraulic properties using X-ray Computed Tomography and image-based modeling**. *Water Resour. Res.* 51 (2015), 1006–1022. DOI: 10.1002/2014WR016020 (see page 56).

[75] Mao H.; Kumi F.; Li Q. and Han L. **Combining X-ray computed tomography with relevant techniques for analyzing soil–root dynamics – an overview**. *Soil & Plant Science* 66 (2013), 1–19. DOI: 10.1080/09064710.2015.1067711 (see page 57).

[76] Anderson S.; Gantzer C. **Determination of soil water content by X-ray computed tomography and magnetic resonance imaging**. *Irrigation Science* 10 (1987), 63–71. DOI: 10:63-71 (see page 57).

[77] Metzner R.; Eggert A.; van Dusschoten D.; Pflugfelder D.; Gerth S.; Schurr U.; Uhlmann N. and Jahnke S. **Direct comparison of MRI and X-ray CT technologies for 3D imaging of root systems in soil: potential and challenges for root trait quantification**. *Plant Methods* (2015), 11–17. DOI: 10.1186/s13007-015-0060-z (see page 57).

[78] Arias J.; Peralta-Videa J.; Ellzey J.; Ren M.; Viveros M.; Gardea-Torresdey J. **Effects of Glomus deserticola inoculation on Prosopis: enhancing chromium and lead uptake and translocation as confirmed by X-ray mapping**. *Environ Exp Bot* 68:2 (2010), 139–148. DOI: 10.1186/s13007-015-0060-z (see page 57).

[79] Hapca S.; Wang Z.; Otten W.; Wilson C.; Baveye P. **Automated statistical method to align 2D chemical maps with 3D X-ray computed micro-tomographic images of soils**. *Geoderma*: 164 (2011), 146–154 (see page 57).

[80] Goethals P.; Volkaert A.; Jacobs P.; Roels S.; Carmeliet J. **Comparison of Positron Emission Tomography and X-ray radiography for studies of physical processes in sandstone**. *Engineering Geology*: 103 (2009), 134–138 (see page 57).

[81] Pelc N. **Recent and Future Directions in CT Imaging**. *Ann Biomed Eng*. 42:2 (1975), 260–268. DOI: 10.1007/s10439-014-0974-z (see page 57).

[82] Bengio Y.; Courville A.; Vincent P. **Representation learning: A review and new perspectives**. *IEEE Trans. Pattern Anal. Mach. Intell*. 35 (2013), 1798–1828. DOI: 10.1109/TPAMI.2013.50 (see page 58).

A) Permafrost core samples characteristics

Table A1: Physical characteristics of cut permafrost core samples measured and written in the frozen laboratory

Sample	Depth (start) [cm]	Thickness (cm)	Depth (end) [cm]	Mean depth [cm]	diameter [cm]	Volume [cm³]	weight of sample bag [g]	wet weight (incl. bag) [g]
KUR17-C001_1	0.0	-	20.00	10.0	7.50	-	19.45	366.72
KUR17-C001_2	20.3	0.99	21.29	20.8	7.50	43.7	3.83	62.19
KUR17-C001_3	21.3	0.78	22.08	21.7	7.50	34.5	4.19	47.01
KUR17-C001_4	22.5	1.10	23.60	23.1	7.50	48.6	4.17	53.93
KUR17-C001_5	23.5	0.95	24.45	24.0	7.50	42.0	4.14	49.21
KUR17-C001_6	24.6	0.98	25.58	25.1	7.50	43.3	4.16	53.97
KUR17-C001_7	25.7	0.97	26.67	26.2	7.50	42.9	4.22	48.52
KUR17-C001_8	26.8	0.90	27.70	27.3	7.50	39.8	4.14	55.37
KUR17-C001_9	28.0	0.65	28.65	28.3	7.50	28.7	4.21	39.49
KUR17-C001_10	28.7	0.92	29.62	29.2	7.50	40.6	4.20	48.67
KUR17-C001_11	29.9	0.85	30.75	30.3	7.50	37.6	4.20	43.75
KUR17-C001_12	30.8	0.87	31.67	31.2	7.50	38.4	4.22	51.96
KUR17-C001_13	31.9	0.77	32.67	32.3	7.50	34.0	4.16	53.00
KUR17-C001_14	32.9	1.65	34.55	33.7	7.50	72.9	4.12	110.24
KUR17-C001_15	34.7	1.90	36.60	35.7	7.50	83.9	4.21	126.26
KUR17-C001_16	36.6	1.95	38.55	37.6	7.50	86.1	4.21	134.55
KUR17-C001_17	38.6	1.95	40.55	39.6	7.50	68.5	4.20	89.81
KUR17-C001_18	40.5	1.50	42.00	41.3	7.50	66.3	4.19	84.71
KUR17-C001_19	42.7	2.08	44.78	43.7	7.50	91.9	4.20	118.65
KUR17-C001_20	45.0	1.78	46.78	45.9	7.50	78.6	4.21	106.94
KUR17-C001_21	46.9	2.20	49.10	48.0	7.50	97.2	4.20	103.57
KUR17-C001_22	49.3	2.10	51.40	50.4	7.50	92.8	4.18	111.50
KUR17-C001_23	51.5	1.96	53.46	52.5	7.50	86.6	4.19	108.31
KUR17-C001_24	53.6	2.11	55.71	54.7	7.50	93.2	4.19	111.69
KUR17-C001_25	55.8	1.90	57.70	56.8	7.50	83.9	4.19	107.40
KUR17-C001_26	57.8	1.95	59.75	58.8	7.50	86.1	4.19	101.16
KUR17-C001_27	59.9	2.16	62.06	61.0	7.50	95.4	4.19	128.15
KUR17-C001_28	62.1	1.95	64.05	63.1	7.50	86.1	4.19	117.89
KUR17-C001_29	64.3	2.14	66.44	65.4	7.50	94.5	4.19	129.28
KUR17-C001_30	66.6	2.12	68.72	67.7	7.50	93.7	4.19	128.61
KUR17-C001_31	68.9	2.12	71.02	70.0	7.50	93.7	4.19	119.60
KUR17-C001_32	71.0	1.40	72.40	71.7	7.50	61.9	4.19	76.42
KUR17-C001_33	73.0	1.50	74.50	73.8	7.50	66.3	4.19	96.26
KUR17-C001_34	75.2	2.08	77.28	76.2	7.50	91.9	4.19	129.77
KUR17-C001_35	77.5	2.06	79.56	78.5	7.50	91.0	4.19	119.73
KUR17-C001_36	79.7	2.08	81.78	80.7	7.50	91.9	4.19	128.50
KUR17-C001_37	81.8	2.04	83.84	82.8	7.50	90.1	4.19	125.38
KUR17-C001_38	84.1	2.10	86.20	85.2	7.50	92.8	4.19	123.77
KUR17-C001_39	86.3	1.80	88.10	87.2	7.50	79.5	4.19	80.67
KUR17-C001_40	88.3	1.95	90.25	89.3	7.50	86.1	4.19	74.82
KUR17-C001_41	90.5	1.20	91.70	91.1	7.50	53.0	4.19	51.02
KUR17-C001_42	93.5	1.28	94.78	94.1	7.50	56.5	4.19	48.86
KUR17-C001_42-a)	-	-	-	97.0	-	-	4.19	28.54
KUR17-C001_43	99.0	1.98	100.98	100.0	7.50	87.5	4.19	74.79
KUR17-C001_44	101.1	2.05	103.15	102.1	7.50	90.6	4.19	81.59
KUR17-C001_44a)	-	-	-	104.0	-	-	4.19	53.45
KUR17-C001_44-45-extra	-	-	-	106.0	-	-	4.19	18.24
KUR17-C002_45	106.8	2.08	108.88	107.8	7.50	91.9	4.19	86.02
KUR17-C002_46	109.0	2.07	111.07	110.0	7.50	91.4	4.19	84.44
KUR17-C002_47	111.2	2.06	113.26	112.2	7.50	91.0	4.19	83.53
KUR17-C002_48	113.3	2.07	115.37	114.3	7.50	91.4	4.19	85.15
KUR17-C002_49	115.6	2.09	117.69	116.6	7.50	92.3	4.19	86.60
KUR17-C002_50	117.8	2.18	119.98	118.9	7.50	96.3	4.19	84.95
KUR17-C002_50-51 extra	-	-	-	120.0	-	-	4.19	24.40
KUR17-C002_51	121.0	1.60	122.60	121.8	7.50	70.7	4.19	64.50
KUR17-C002_52	122.7	1.62	124.32	123.5	7.50	71.6	4.19	65.09
KUR17-C002_53	124.5	1.55	126.05	125.3	7.50	68.5	4.19	64.03
KUR17-C002_53 a extra	130.0	-	135.00	132.5	-	-	4.19	42.20
KUR17-C002_53 b extra	130.0	-	135.00	132.5	-	-	4.19	60.50
KUR17-C002_54	136.5	2.20	138.70	137.6	7.50	97.2	4.19	85.02
KUR17-C002_55	138.8	2.21	141.01	139.9	7.50	97.6	4.19	85.00
KUR17-C002_56	141.0	-	146.00	143.5	-	-	4.19	99.80
KUR17-C002_57	147.1	2.21	149.31	148.2	7.50	97.6	4.19	86.26
KUR17-C002_58	149.4	2.23	151.63	150.5	7.50	98.5	4.19	90.86
KUR17-C002_59	155.0	1.90	156.90	156.0	7.50	83.9	4.19	67.53
KUR17-C002_60	157.0	1.84	158.84	157.9	7.50	81.3	4.19	78.50
KUR17-C002_61	158.7	2.05	160.75	159.7	7.50	90.6	4.19	92.35
KUR17-C002_62	162.6	2.67	165.27	163.9	7.50	118.0	4.19	111.23
KUR17-C002_63-extra	-	-	-	166.0	-	-	4.19	44.85
KUR17-C002_64	167.0	-	173.00	170.0	-	-	10.71	180.18
KUR17-C002_65	174.0	-	181.00	177.5	-	-	10.71	203.56
KUR17-C002_66	181.0	-	184.00	182.5	-	-	4.19	59.60

Selbstständigkeitserklärung

Hiermit versichere ich, dass ich die vorliegende wissenschaftliche Arbeit selbstständig und ohne Hilfe Dritter verfasst habe. Andere als die angegebenen Quellen und Hilfsmittel wurden nicht verwendet. Die den benutzten Quellen wortlich oder inhaltlich entnommenen Abschnitte sind als solche kenntlich gemacht. Diese wissenschaftliche Arbeit hat in gleicher oder aehnlicher Form noch keiner Pruefungsbehoerde vorgelegen und wurde auch nicht veroeoffentlicht.

Autor	Damir Gadylyaev
Matrikelnummer	798578
Universitaet	University of Potsdam
Studiengang	Remote Sensing, geoInformation and Visualization
Titel	Applying Computed Tomography (CT) scanning forsegmentation of permafrost constituents in drill cores

_____   _____

Ort, Datum   Damir Gadylyaev